BRNO UNIVERSITY OF TECHNOLOGY

VYSOKÉ UČENÍ TECHNICKÉ V BRNĚ

FACULTY OF ELECTRICAL ENGINEERING AND COMMUNICATION

FAKULTA ELEKTROTECHNIKY
A KOMUNIKAČNÍCH TECHNOLOGIÍ

DEPARTMENT OF RADIO ELECTRONICS

ÚSTAV RADIOELEKTRONIKY

3D PRINTED DIELECTRIC RESONATOR ANTENNA

3D TIŠTĚNÁ DIELEKTRICKÁ REZONÁTOROVÁ ANTÉNA

BACHELOR'S THESIS

BAKALÁŘSKÁ PRÁCE

AUTHOR — Masauso Lungu

AUTOR PRÁCE

SUPERVISOR — Ing. Jaroslav Zechmeister

VEDOUCÍ PRÁCE

BRNO 2022

Bachelor's Thesis

Bachelor's study program **Electronics and Communication Technologies**

Department of Radio Electronics

Student: Masauso Lungu ***ID:*** 209533

Year of study: 3 ***Academic year:*** 2021/22

TITLE OF THESIS:

3D printed dielectric resonator antenna

INSTRUCTION:

Learn about the principle and design of dielectric resonator antennas and their feeding possibilities. In CST Microwave Studio create a numerical model of the cylindrical dielectric resonator antenna for the 5.8 GHz ISM band. Investigate the effect of different types of antenna feeding on the antenna characteristics. In consultation with the supervisor, select the appropriate type of antenna feeding and complete the antenna design.

For the designed antenna, simulate the influence of the manufacturing process on antenna properties. Fabricate the proposed antenna using 3D printing technology using different printing patterns. Measure the fabricated antenna and compare it with the simulation results.

RECOMMENDED LITERATURE:

[1] PETOSA, A., Dielectric Resonator Antenna Handbook. Boston: Artech House, 2007. Artech House Antennas and Propagation Library. ISBN 1-59693-206-6.

[2] PROCHÁZKA, M., Antény: encyklopedická příručka. 2. vyd. Praha: BEN - technická literatura, 2001. ISBN 80-7300-028-8.

Date of project specification: 11.2.2022 ***Deadline for submission:*** 1.6.2022

Supervisor: Ing. Jaroslav Zechmeister

doc. Ing. Lucie Hudcová, Ph.D.
Chair of study program board

ABSTRACT

This bachelor's thesis deals with the design and fabrication of a cylindrical dielectric resonator antenna operating at the frequency band of ISM 5.8GHz. In this work, various antenna feeding methods are described. In CST microwave studio, two numerical models of the cylindrical dielectric resonator antenna, one with a coaxial probe and the other with aperture coupling were designed and investigated. The model with aperture coupling was then fabricated using 3D printing technology and subsequently, its properties were measured and verified with the simulated results.

KEYWORDS

Dielectric resonator, Dielectric resonator antenna, cylindrical dielectric resonator antenna, 3D printing, 3D printed antenna, CST Microwave Studio.

ABSTRAKT

Tato bakalářská práce se zabývá návrhem a výrobou válcové dielektrické rezonátorové antény pracující na kmitočtové pásmu ISM 5,8GHz. V této práci jsou popsány různé metody buzení antény. V CST Microwave Studio byly navrženy a prozkoumány dva numerické modely válcové dielektrické rezonátorové antény, jeden s koaxiální sondou a druhý se štěrbinovým napajení. Model se štěrbinovým napajení byl poté vyroben technologií 3D tisku a následně byly jeho vlastnosti změřeny a ověřeny simulovanými výsledky.

KLÍČOVÁ SLOVA

Dielektrický rezonátor, dielektrická rezonátorová anténa, válcová dielektrická rezonátorová anténa, 3D tisk, 3D tištěné antény, CST Microwave Studio

ROZŠÍŘENÝ ABSTRAKT

Cílem předložené bakalářské páce bylo seznámit se s principem a návrhem dielektrických rezonátorových antén a možnostmi jejich buzení. Nasledně narvhnout válcovou dielektrickou rezonátorovou anténu pro kmitočtové pásmo ISM 5,8 GHz a vyrobit navrženou anténu pomocí technologie 3D tisku.

V rámci teto práce byly nejprve navrženy dva numerické modely válcové dielektrické rezonátorové antény, jeden s koaxialní sondou a druhý se štěrbinovým napajením a jejich parametry byly simulované (viz kapitole 4). Při návrhu modelů antén bylo použito CST micowave studio. Navrhovane antény byly simulované taky, aby dosahly přizpůsobeného modulu činitele odrazu pod hodnotu -10 dB. Nasledně, byly zkoumaný vlivy fyzických parametrů na vlastnost dielctrické rezánatorové antény pro tyto konfigurace. Při srovnaní dosažených vysledků, knofigurace s koaxialní sondou měla celkem lepší vysledky než ten se štěrbinovým napajením (viz 4.3). Avšak, změna fyzických parametrů antén ukazovala podobný vliv na funkce antény u obou konfigurací. Nejzásadnější vliv měla změna rozměrů dielektrického rezantoru.

Z důvodu zjednodušeného výrobního procesu byla pro výrobu zvolena konfigurace se štěrbinovým napajením. Zvolena anténa byla dále optimalizována pro vyrobu a anténa byla vyrobena pomocí Prusa i3 MK3S 3D tisku. Celkem 4 antény byly vyrobené s ruznými tiskovými profily a nasledně byly změřeny paramentry antén.

Měření na první pokus nedopadlo dobře, rezonanční kmitočet pro všechny modely byl posunut na vyšší kmitočet mimo pasmo ISM 5,8 GHz, než pro který byla antena navržena(viz 5.6). Posun rezonančního kmitočtu mimo cíl byl způsoben menší vyslednou dielektrickou konstantou materialu nez byla uvedena v katalogovém listu. Po nutných úpravách anteny s novými hodnotami dielektrické konstanty, bylo dosaženo lepších vysledků činitele odrazu. Mezi 4 profily tisku, model s rectilinear profilem měl nejlepší vysledky (podkapitole 5.3.3). Práce byla dokočena měřením směrové charakteristky ve stíněné komoře.

LUNGU, Masauso. *3D printed dielectric resonator antenna*. Brno: Brno University of Technology, Faculty of Electrical Engineering and Communication, Department of Radio Electronics, 2022, 62 p. Bachelor's Thesis. Advised by Ing. Jaroslav Zechmeister

Author's Declaration

Author:	Masauso Lungu
Author's ID:	209533
Paper type:	Bachelor's Thesis
Academic year:	2021/22
Topic:	3D printed dielectric resonator antenna

I declare that I have written this bachelor's thesis independently, under the guidance of the advisor and using exclusively the technical references and other sources of information cited in the thesis and listed in the comprehensive bibliography at the end of the thesis.

As the author, of the I furthermore declare that, with respect to the creation of this thesis, I have not infringed any copyright or violated anyone's personal and/or ownership rights. In this context, I am fully aware of the consequences of breaking Regulation § 11 of the Copyright Act No. 121/2000 Coll. of the Czech Republic, as amended, and of any breach of rights related to intellectual property or introduced within amendments to relevant Acts such as the Intellectual Property Act or the Criminal Code, Act No. 40/2009 Coll. of the Czech Republic, Section 2, Head VI, Part 4.

Brno ....

author's signature*

*The author signs only in the printed version.

ACKNOWLEDGEMENT

I would like to thank my supervisor Ing. Jaroslav Zechmeister for giving me the opportunity to work under his supervision and his valuable advise throughout the course of this thesis.

Contents

List of Figures

List of Tables

Introduction

The advancement in wireless communication has led to an increase in demand of small and compact electronic devices such as smartphones. It is undeniable fact that wireless communication is now part of our daily lives in most parts of the world. However, today's market demands electronic systems of higher efficiency, wide bandwidth, and reduced equipment size. Meeting these demands is a major challenge in RF and wireless domain as it requires the design of suitably small antennas to be embedded into consumer product as small as earbuds [10, 11].

To mitigate the aforementioned challenges and demands, dielectric resonators (DR's) have proved themselves to be the perfect candidate for antenna application by virtue of their high radiation efficiency, flexible feeding mechanism, a variety of simple geometric shapes, small size and their ability to produce different radiation patterns using different modes [4, 11, 12]. These attractive features also make the dielectric resonator antennas (DRA's) as an alternative to conventional and metallic antennas such as microstrip patch antennas especially for application at millimeter wave frequencies and beyond. This is mainly attribute to the fact that DRA's do not suffer from conduction losses and are characterized by high radiation efficiency when excited properly [3, 4, 10].

Additionally, the advancement in 3D printing technologies have demonstrated their abilities to produce high-performance microwave and millimetre wave passive devices [13]. In recent years, 3D printing technology has been receiving great attention for a wide variety of applications for cost effectiveness, eco-friendliness, and process simplicity in complicated structures. This development has widened the possibilities for further exploitation of the dielectric resonator antennas, as prototypes of different structures with different materials can be quickly fabricated and investigated at a lower cost than ever before [14, 15].

In this thesis, a cylindrical dielectric resonator antenna (CDRA) is designed to operate at frequency band of ISM 5.8 GHz. The antenna is designed and configured in CST microwave studio, two feeding common feeding mechanisms are exploited in order to realize the most suitable method for exciting the CDRA and the resultant antenna is fabricated using 3D printing technology.

The thesis is divided into four chapters. Chapter 1 and 2 gives a theoretical background of dielectric resonator antennas. An overview of 3D printing technology is given in chapter 3. Chapter 4 focuses on design and configuration of the numerical models of the cylindrical dielectric resonator antenna and finally, chapter 5 is aimed at fabrication of the prototype, measurements and discussion of the achieved results.

1 Dielectric resonator antennas

1.1 Introduction

The birth of dielectric resonator antennas followed the introduction and development dielectric resonators, which are nonmetallic dielectric objects that can function as energy devices due to their high dielectric constant ε_r (usually ceramic materials) and a high quality factor (Q-factor) [1, 3, 6, 12]. Dielectric resonators have been used in circuit applications, such as filters and oscillators, offering a more compact alternative to the waveguide cavity resonators and more flexible technology for printed circuit integration [5, 12, 16].

1.2 Major characteristics of dielectric resonator antennas

In general, Dielectric resonator antennas have a number of desirable features: [2, 3, 4, 6, 10, 11, 12, 16, 17]

- Are efficient radiators, especially when compared to microstrip antennas; they do not generate surface waves and they radiate in all directions, but the grounded part, whereas microstrip antennas mainly radiate through their leading and trailing sides.
- Their sizes are proportional to the ratio $\lambda_0/\sqrt{\varepsilon_r}$, where λ_0 denotes the free space wavelength at resonant frequency and ε_r is the dielectric constant of the material.
- Are wideband (typically BW $\cong$ 10%), especially when compared to microstrip antennas, with some geometries achieving BW of 50% or higher.
- By selecting a dielectric material with low-loss characteristics, a high-radiation efficiency can be maintained, even at millimeter-wave frequencies, due to the absence of surface waves and minimal conductor losses associated with the DRAs.
- Are versatile, as different shapes (Fig. 1.1) can be used to excite various modes of different radiation characteristics.
- Can be excited by different feeding mechanism, such as probe, microstrip lines, slots, and coplanar waveguides.
- Can be designed to operate on over a wide range of frequencies (about 1 to 60 GHz).

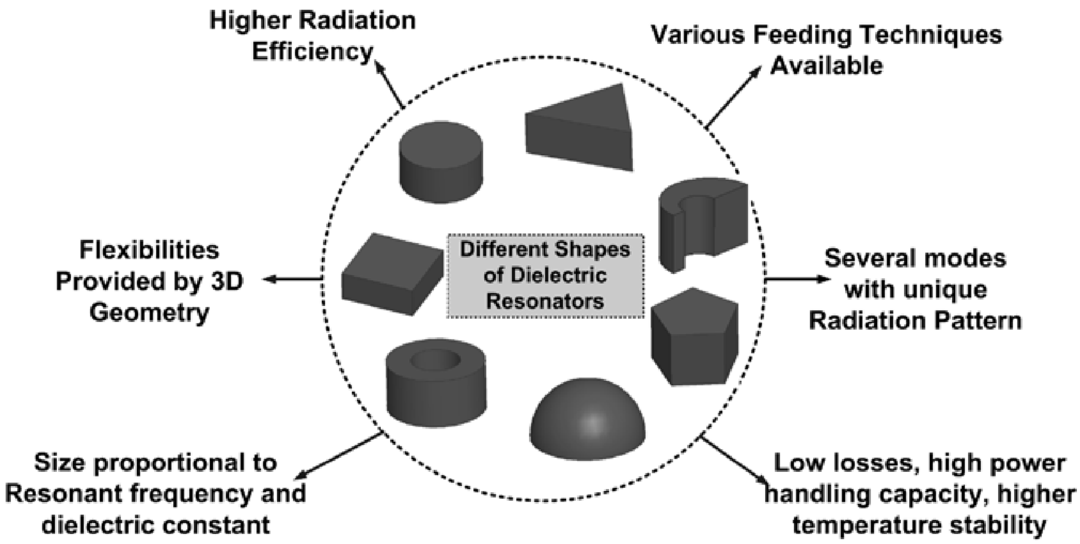

Fig. 1.1: Different Shapes of DRs [1]

1.3 Feeding mechanism of dielectric resonator antennas

In this section, some of the most used feeding mechanisms are discussed.

1.3.1 Aperture coupling

Aperture coupling is the most popular methods used to excite various modes of the DRA because of easy of fabrication [17]. The aperture consist of a slot placed on the ground plane, where the DR is mounted and a transmission line (either miscrostrip, coaxial probe or a waveguide) beneath the ground plane. Different shapes for the aperture slot are used, such as rectangular slots, C-shaped, annular, and cross-shaped slots. Fig. 1.2 shows an example of the rectangular aperture slot. This feeding mechanism offers the advantage of having the feeding network located below the ground plane, thereby isolating the radiating aperture from any unwanted coupling or spurious radiation from the feed line [2, 3, 4, 10, 12]

1.3.2 Coaxial Probe feeding

The coaxial probe is another commonly used feeding mechanism to excite the DRA. This technique involves the use of the centre pin of the coaxial feeding line, which can be placed either adjacent to the DR or embedded inside it. Depending on the

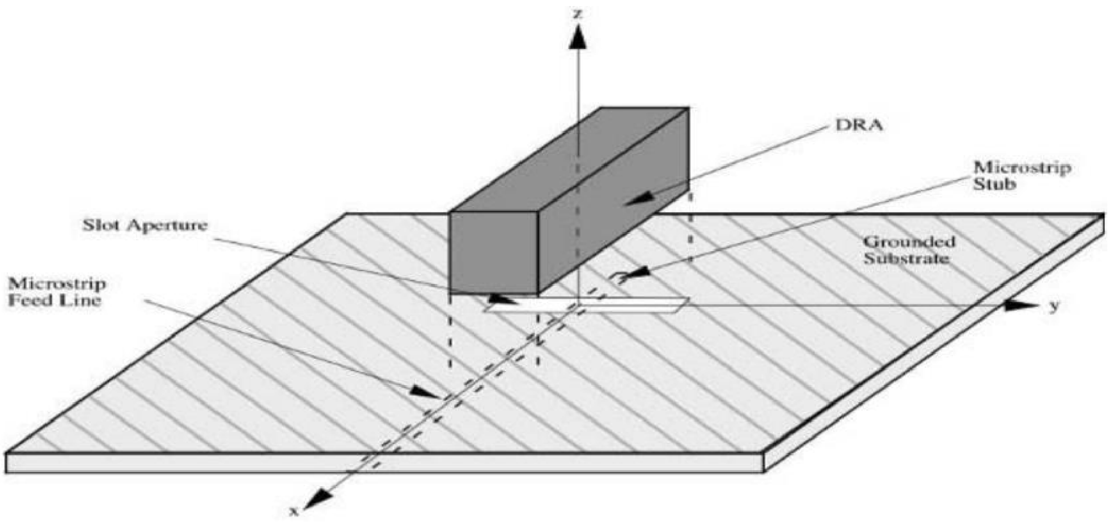

Fig. 1.2: Aperture coupling in DRA[2]

location of the probe, various modes can be excited, and the amount of coupling can be optimized by adjusting the height of the probe (Fig. 1.3).

One major advantage of using the coaxial probe is that is can be directly matched to 50Ω characteristic impedance. However, the practical disadvantage of this technique is the drilling of holes on the ground plane, including the DR itself, which may alter the radiation pattern of the antenna [2, 3, 4, 6, 10, 12, 18].

1.3.3 Microstrip line feeding

This feeding mechanism is realized by using a microstrip, which can be placed either next to or below the DR. Fig. 1.4 shows this feeding technique applied to DRAs. The position and and length of the feed line can be used to achieve a controlled coupling. However, with this method, the degree of coupling can be affected by the dielectric constant ε_r of the DR. Strong coupling can be achieved for higher values ($\varepsilon_r > 20$), while at lower values, the maximum amount of coupling is significantly reduced, which can be problematic if low dielectric constant values are required for obtaining wideband operation [2, 3, 4, 10, 12]

1.3.4 Coplanar coupling

Fig. 1.5 shows an example of coplanar coupling. Open-circuit coplanar waveguides can be used to directly feed DRAs, like microstrip open-circuit microstrip lines. The coupling level can be adjusted by positioning the DR over the loop of the coplanar [2, 3, 4, 12].

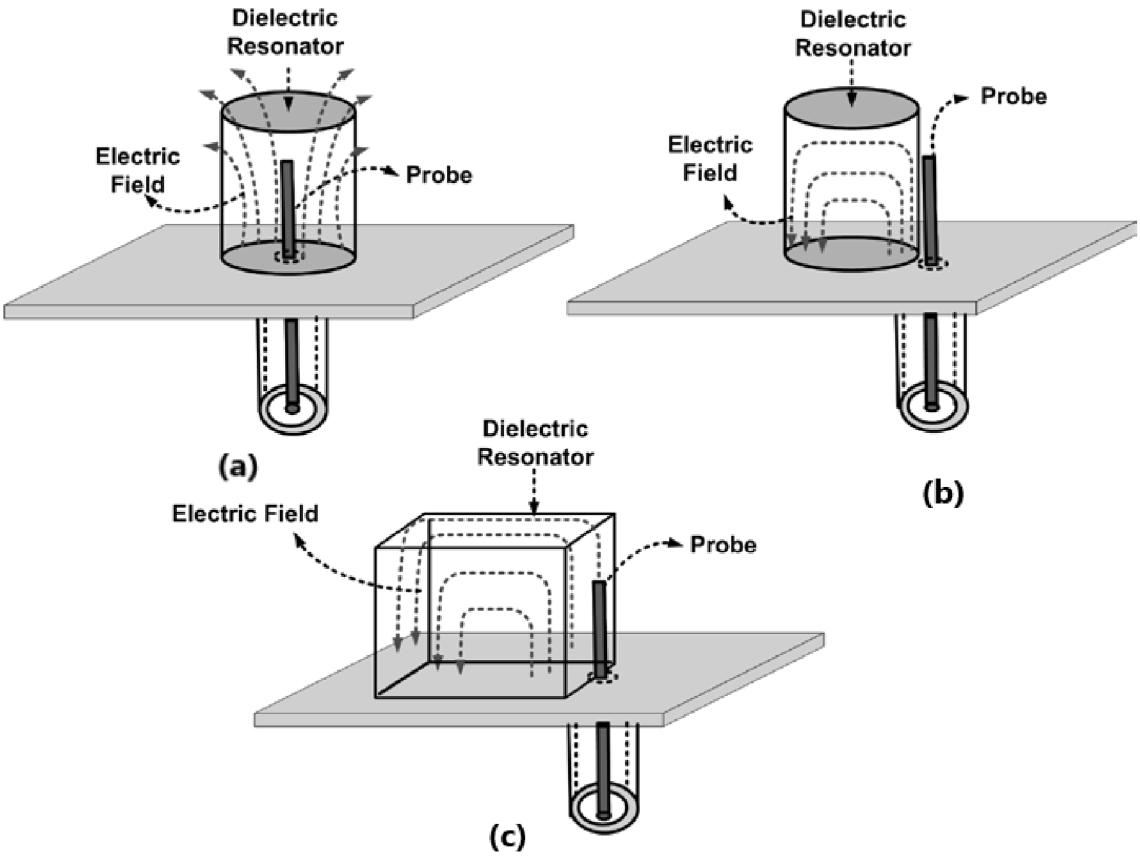

Fig. 1.3: Exciting different modes in DRAs by placing probes at different location[3]

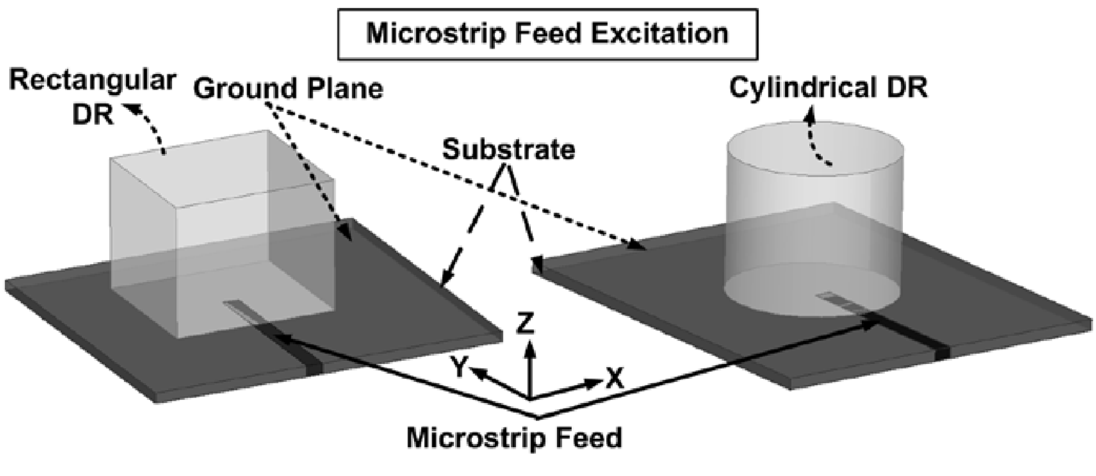

Fig. 1.4: Exciting of rectangular and cylindrical DRA using microstrip feed[3]

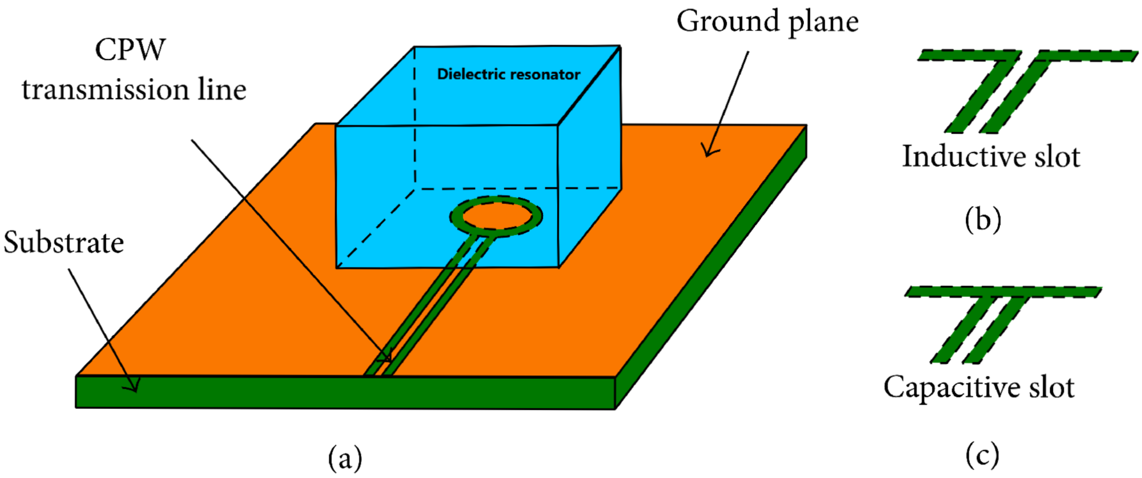

Fig. 1.5: Coplanar-waveguide coupling[4]

2 The Cylindrical dielectric resonator antenna (CDRA)

This chapter focuses on the details of the cylindrical form of the DRAs and its parameters.

2.1 Parameters of the CDRA

The cylindrical DRA is characterized by the height h and the radius a and the dielectric constant ε_r as shown in Fig. 2.1. The aspect ratio a/h, which determines $k_0 a$ (k_0 is the free space wave number) and the Q-factor for the given dielectric constant, gives the designer the degree of flexibility in designing the CDRA by choosing the most suitable aspect ratio to best achieve the required frequency and bandwidth [4, 5, 12, 19, 20].

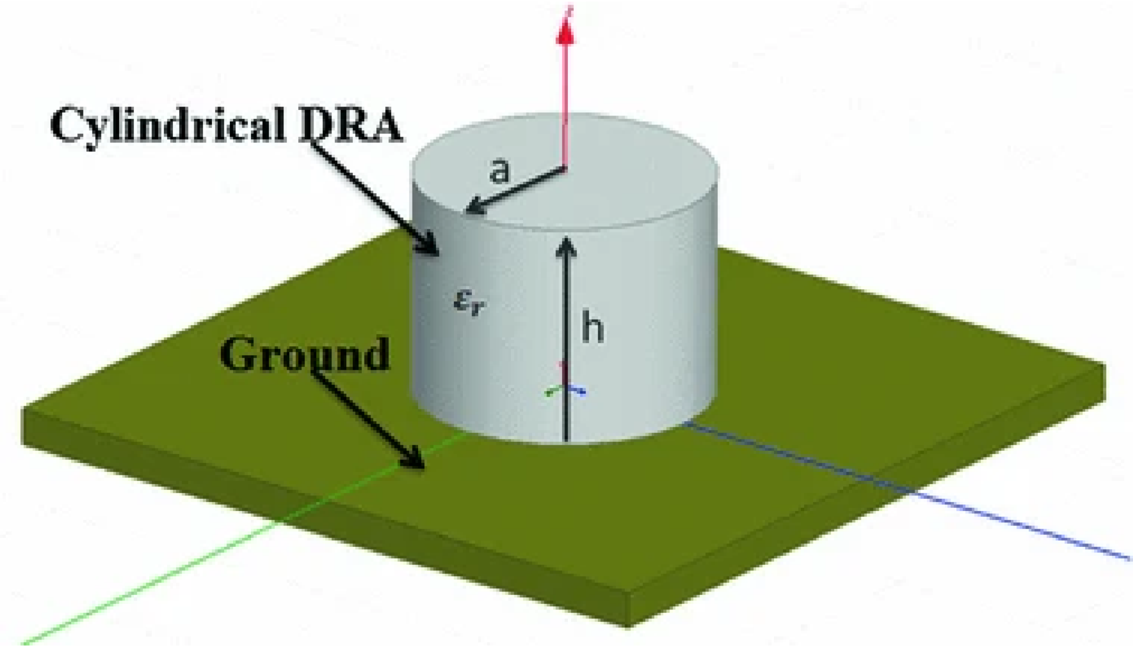

Fig. 2.1: Parameters of the cylindrical DRA[5]

2.2 Resonant frequency and radiation Q-factor of the lower-order modes of the CDRA

This section describes the resonant frequency f_r and the radiation Q-factor of the three most used lower order modes of the CDRA. The three modes are $TE_{01\delta}$,

$TM_{01\delta}$ and hybrid $HE_{11\delta}$ modes [6, 12]. Fig. 2.2 shows the visualization of the three lower order modes. The equations for the resonant frequency and Q-factor for the aforementioned modes are given in the following next subsections, the equations are based on expressions from [6], [11] and [12]. The type of mode to be excited depends on the kind of the feeding technique and the placement of the feed being used.

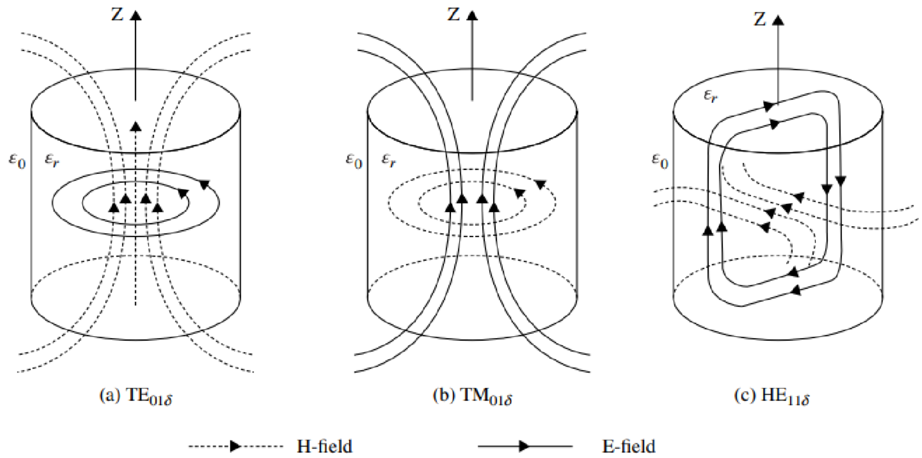

Fig. 2.2: Radiation pattern of the lower order modes of the CDRA[6]

2.2.1 $TE_{01\delta}$ Mode

$$f_r = \frac{c}{2\pi a}\left(\frac{2.327}{\sqrt{\varepsilon_r + 1}}\right)\left[1 + 0.2123\left(\frac{a}{h}\right) - 0.00898\left(\frac{a}{h}\right)^2\right]; \quad 0.125 \le \frac{a}{h} \le 5 \qquad (2.1)$$

$$Q = 0.078192\,(\varepsilon_r)^{1.27} \times \left[1 + 17.31\left(\frac{h}{a}\right) - 21.57\left(\frac{h}{a}\right)^2 + 10.86\left(\frac{h}{a}\right)^3 - 1.98\left(\frac{h}{a}\right)^4\right]; \quad 0.5 \le \frac{a}{h} \le \qquad (2.2)$$

2.2.2 $TM_{01\delta}$ Mode

$$f_r = \frac{c}{2\pi a}\left(\frac{1}{\sqrt{\varepsilon_r + 2}}\right)\sqrt{\left[(3.83)^2 + \left(\frac{\pi}{2}\right)^2\left(\frac{a}{h}\right)^2\right]}; \quad 0.125 \le \frac{a}{h} \le 5 \qquad (2.3)$$

$$Q = 0.00872\,(\varepsilon_r)^{0.888}\,e^{0.03975\varepsilon_r}\left[1 + \left(0.3 - 0.2\left(\frac{a}{h}\right)\right)\left(\frac{38-\varepsilon_r}{28}\right)\right] \times \left(0.9498\left(\frac{a}{h}\right) + 2,058.33\left(\frac{a}{h}\right)^{4.3226} e^{3.501\left(\frac{a}{h}\right)}\right); \quad 0.5 \le \frac{a}{h} \le 5 \qquad (2.4)$$

2.2.3 HE$_{11\delta}$ mode

$$f_r = \frac{c}{2\pi a}\left(\frac{6.324}{\sqrt{\varepsilon_r + 2}}\right)\left(0.27 + 0.18\left(\frac{a}{h}\right) + 0.005\left(\frac{a}{h}\right)^2\right); \quad 0.125 \leq \frac{a}{h} \leq 5 \tag{2.5}$$

$$Q = 0.01\left(\frac{a}{h}\right)^{1.3}\left[1 + 100e^{-2.05\left(0.5\left(\frac{a}{h}\right) - 0.0125\left(\frac{a}{h}\right)^2\right)}\right]; \quad 0.5 \leq \frac{a}{h} \leq 5 \tag{2.6}$$

3 3D printing technology

3D printing technology, also known as additive manufacturing or Digital fabrication technology, refers to the processes used to generate a 3D physical object from a geometrical representation by successive adding materials layer by layer. 3D printing technology, first commercialized in 1984 by Charles Hull, is a fast-emerging technology with increasing application in a wide range of industries, such as healthcare, agriculture, automotive, architecture [7, 8, 21]. One of the many advantages of 3D printing is that it allows the designers to quickly fabricate prototypes of their designs before final products can be manufactured by rather time-consuming expensive processes, thereby giving the designer time to adjust the design if necessary.

Fig. 3.1: Prusa i3 MK3S+ 3D printer[7]

3.1 Types of 3D printing

According to ISO/ASTM52900, seven categories of 3D printing processes are defined [8, 21]:

- Material extrusion
- Powder bed fusion
- Binder jetting
- Direct energy deposition
- Sheet lamination
- Vat photopolymerization
- Material jetting

3.1.1 Material extrusion - FFF/FDM

Material extrusion, also known as Fused Filament Fabrication (FFF) or Fused deposition modeling (FDM) (FDM is a trademark of Stratasys company), is the most wide spread and most affordable 3D printing technology. This technology uses a continuous filament of a thermoplastic, such acrylonitrile butadiene styrene (ABS), as the base material. The filament is fed from a coil, through a moving heated printer extruder head and the heated semi-liquid filament is then deposited on the printing platform layer-by-layer from bottom until the object is completed [7, 8, 21, 22]. The major downside of this technique is that the layers on the printed object are visible, as such material infill is not 100%.

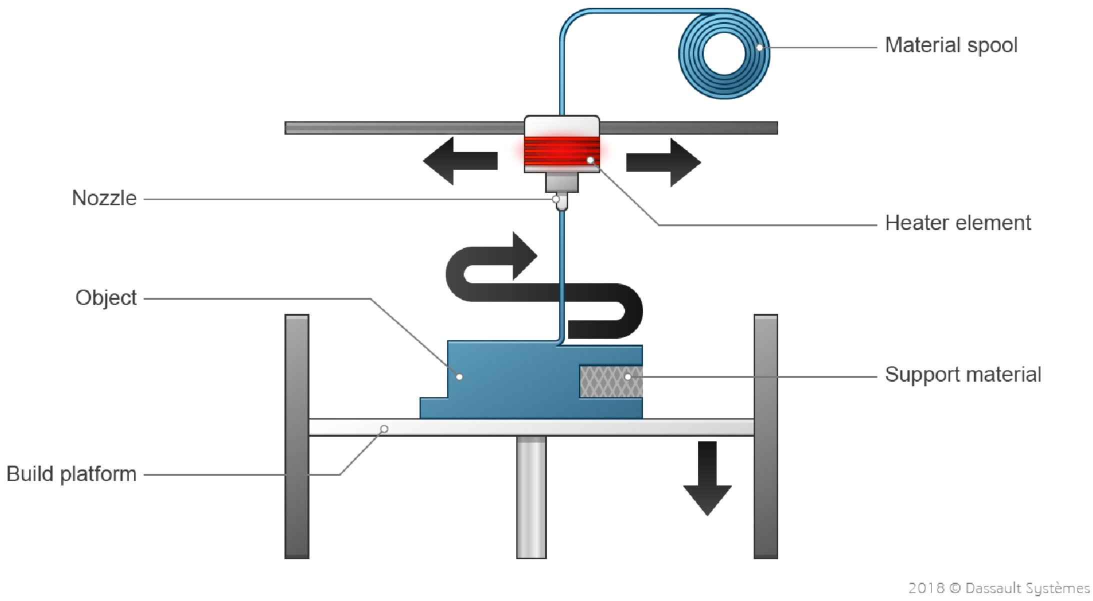

Fig. 3.2: Assembly of material extrusion 3D printer[8]

3.1.2 Vat photopolymerization

Vat photopolymerization is the main 3D printing technique frequently used. The technique refers to curing of photo-reactive polymers by using a laser, light or ultraviolet (UV) [8, 21]. Most vat photopolymerization 3D printing technologies include: Stereolithograthy (SLA), digital light processing (DLP), and daylight polymer printing (DPP).

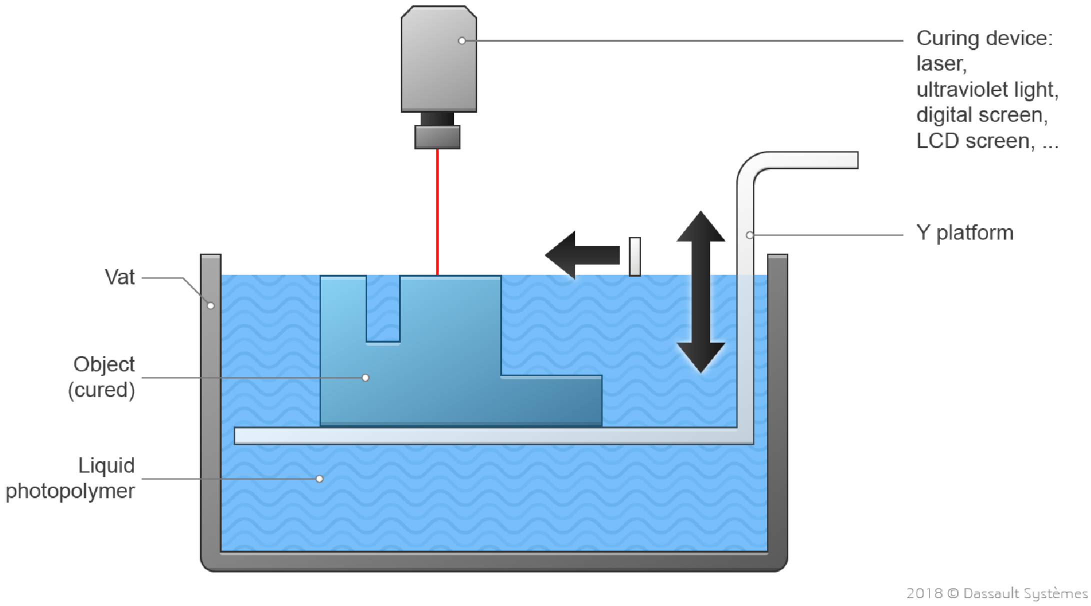

Fig. 3.3: Assembly of vat photopolymerization 3D printer[8]

3.2 Material used for 3D printing

Depending on the type of 3D printing technique, a broad range of materials are used, each one carefully corresponding to the technical requirements of the end product. Most popular materials used include: polymers, ceramics, composites, carbon fibres and sintered powdered metal [8, 21].

4 Numerical model of the CDRA

This chapter focuses on the design and configuration of the numerical models of the CDRA.The CDRA offers a wide range of design options which are influenced by the requirements of the desired mode. In this thesis two numerical models of the CDRA are designed, one with coaxial probe coupling and the other with aperture coupling. For the selected coupling methods, the hybrid mode $\text{HE}_{11\delta}$ is the desired mode to be excited [11, 12].

The antennas are designed in CST Microwave studio (2019 version) and a parametric study on physical parameters of the antenna is conducted to observe the behavior and determine the limits of the two coupling methods on the properties of the antenna.

The antenna models are designed to operate over the frequency band of ISM 5.8 GHz.

4.1 Design aspects of the CDRA

The antenna models presented in this work are each made of a single cylindrical DR placed top of the square shaped ground plane ($60mm \times 60mm \times 1.52mm$). The material used for the DRs is Preperm 1000 (lossy), which has the dielectric constant of $\varepsilon_r = 10$, FR-4 for the substrate ($\varepsilon_s = 4.3$) and an additional thin layer of copper metal on the ground plane (0.035mm thick). Fig. 2.1 shows the geometrical shape of the CDRA.

Initial values for the dimensions of the DR (a and h) were determined manually by evaluating equation 2.5 and 2.6 presented in section 2.2.3 for different combination of a and h for the given range of the aspect ratio $\frac{a}{h}$, which yielded the target resonant frequency $f_r = 5.8$ GHz. The desired dimensions were later confirmed by simulation in CST microwave studio. The hybrid $\text{HE}_{11\delta}$ is taken as the target mode in the following designs, because according to [12], the placement of the feeds used in these designs, will primarily excite $\text{HE}_{11\delta}$.

4.2 CDRA model with coaxial probe

In this section, the design of the CRDA with coaxial probe is described. Achieved simulation and the effect of changing parameters on the antenna properties are presented. The dimensions of the coaxial probe used are based on specifications of the 50Ω LMR-100 coaxial cable [9] given in Fig. 4.1. The coaxial probe is placed adjacent to the DR, so that it can excite the bybrid $\text{HE}_{11\delta}$ mode of the lower order [4, 12, 18]. Initial dimensions for the antenna are given in Tab. 4.1.

Tab. 4.1: Initial dimensions of the probe model

Parameter	Value [mm]
Radius of the resonator a	5.915
Height of the resonator h	8.873
Length of the probe l_p	8.873

Construction Specifications Description	Material	In.	(mm)
Inner Conductor	Solid BCCS	0.018	(0.46)
Dielectric	Solid PE	0.060	(1.52)
Outer Conductor	Aluminum Tape	0.065	(1.65)
Overall Braid	Tinned Copper	0.083	(2.11)
Jacket	See Table	0.110	(2.79)

Fig. 4.1: Specifications of LMR-100A coaxial cable [9]

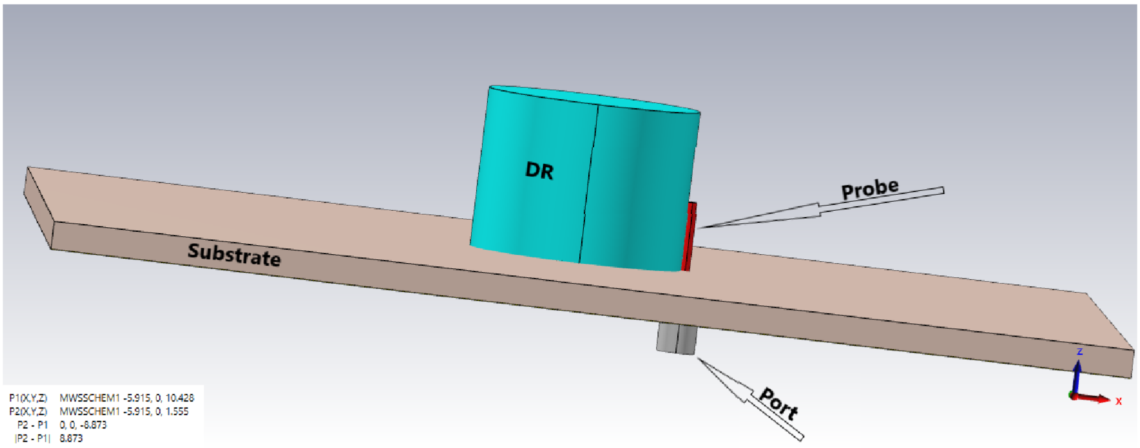

Fig. 4.2: Numerical model of the coaxial probe fed CDRA

4.2.1 Simulation results

During simulation, the probe length was optimized to 3.833 mm above ground. At resonant frequency, the antenna achieved the reflection coefficient of magnitude $|S11| = -38.125$ dB (Fig. 4.3), maximum gain of 5.943 dBi (Fig 4.4), total efficiency of 95.91% (Fig. 4.5) and the operating bandwidth ($|S11| < -10$) of 15.08%. As it can be seen on Fig. 4.6, the antenna radiation is maximum at the top of the DR, which indicate that there was less radiation leakage.

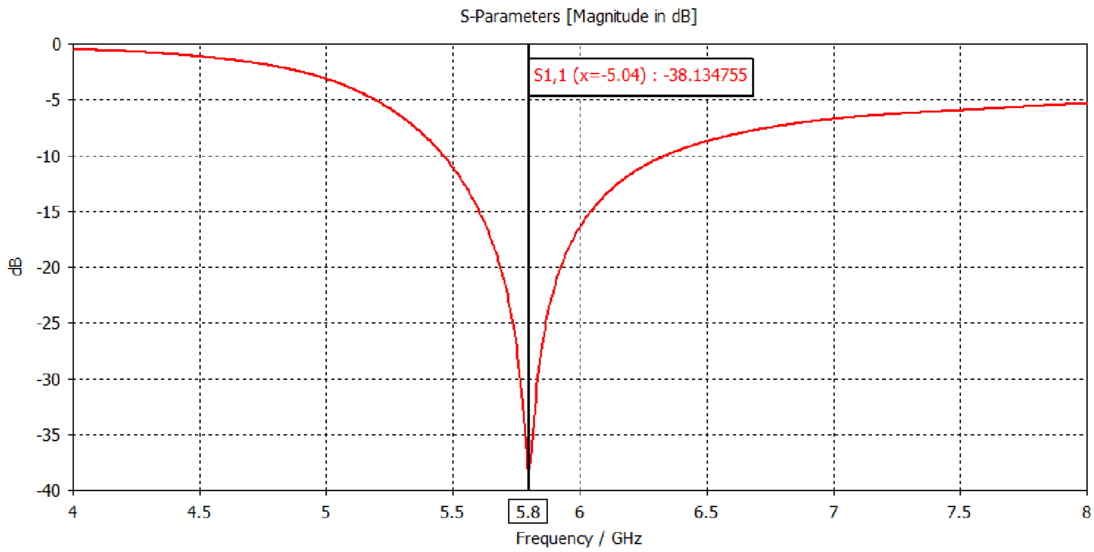

Fig. 4.3: Reflection coefficient for coaxial probe model

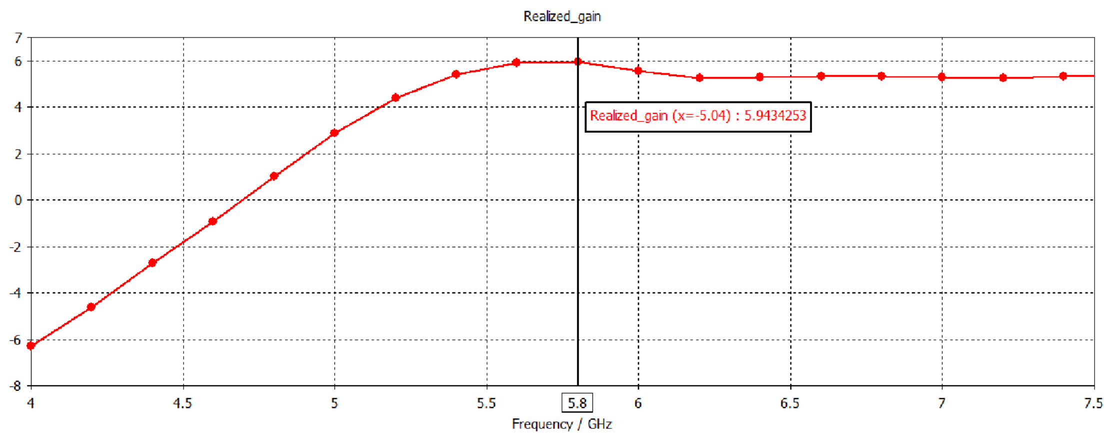

Fig. 4.4: Realized gain for coaxial probe model

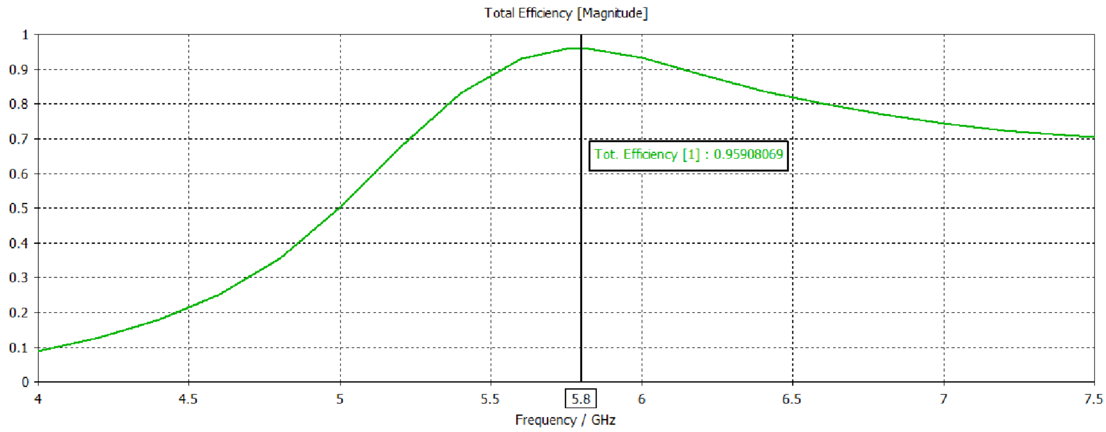

Fig. 4.5: Total efficiency for coaxial probe model

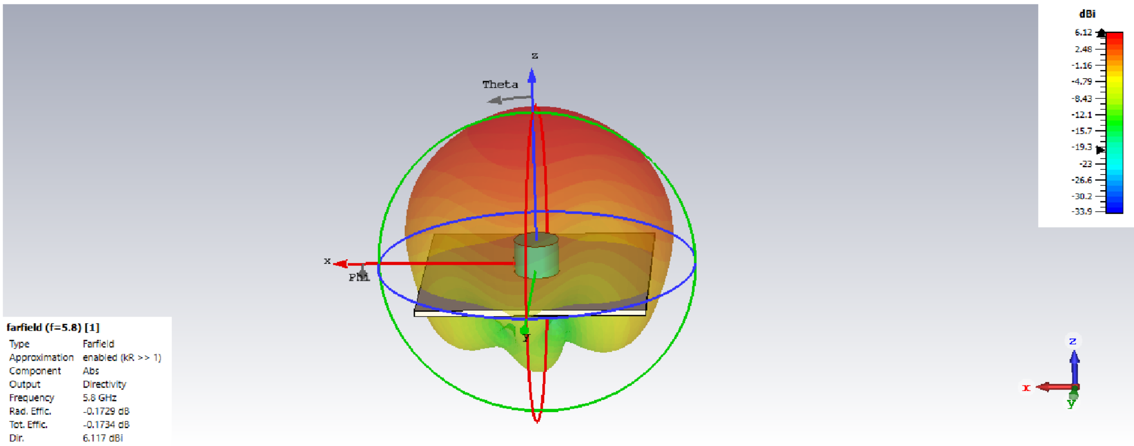

Fig. 4.6: Radiation pattern at 5.8GHz for coaxial probe model

4.2.2 Parametric analysis on coaxial probe model

The effect of varying the dimensions of two main design parameters on the performance of the designed CDRA is studied. The studied parameters are namely the radius of the resonator and the height of the resonator. The parameters are adjusted in the range of +/- 10% of their optimized dimensions and their influence is observed on resonant frequency, fractional impedance bandwidth and realized gain.

As it is evident in Fig 4.8, altering the radius a of the DR greatly affect the behavior of the designed antenna. For example, increasing the radius resulted in shifting the resonant frequency from 5.8 GHz to lower frequencies, whereas reducing the radius resulted in shifting the resonant frequency to higher values. Similarly, altering the height h of the DR causes the shift in resonant frequency, however, the shift is slightly minimal as compared to the case of altering radius (see Fig.4.9). On

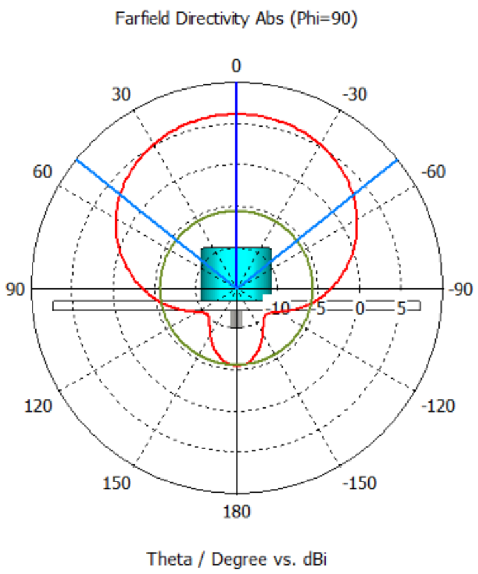

(a) Absolute gain

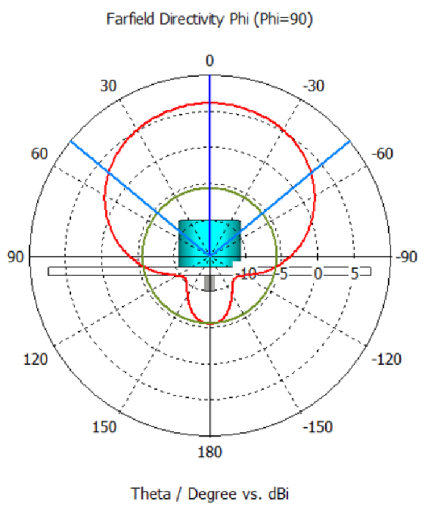

(b) Phi component

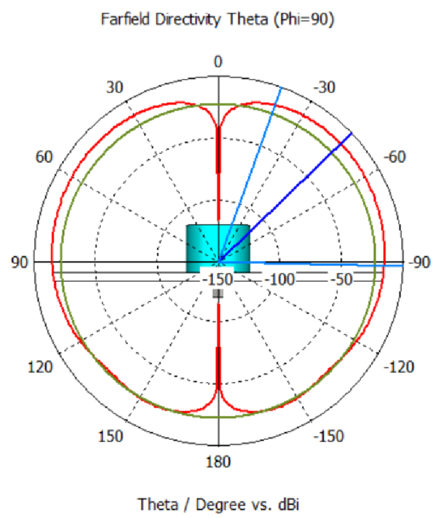

(c) Theta component

Fig. 4.7: Radiation pattern of the coaxial probe model

the other hand, in both cases, effect on maximum achievable gain is less prominent (see Fig. 4.11 and 4.12).

Another parameter that affects the performance of the coaxial probe CDRA is the length of the probe l_p. As it can be seen in Fig. 4.10, increasing or reducing the probe length by a factor x mm alters the operating frequency of the antenna.

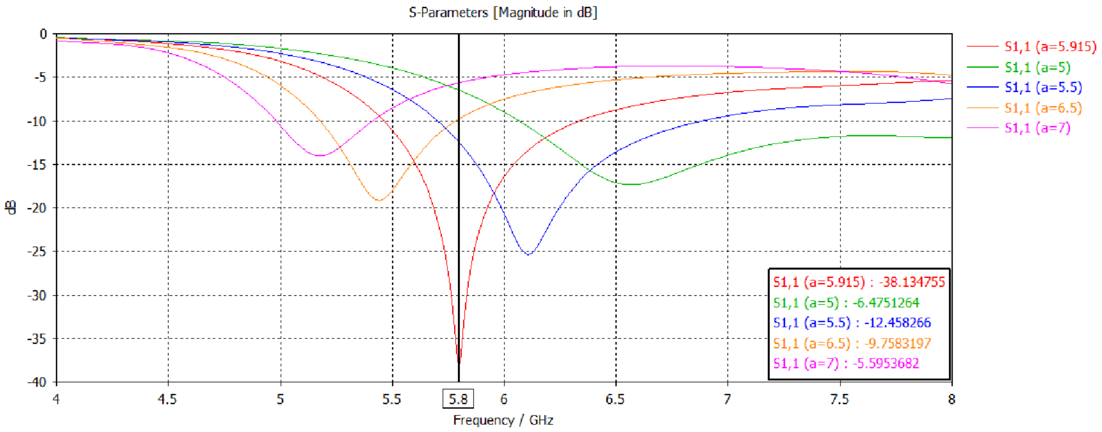

Fig. 4.8: Effect of altering radius of DR on Reflection coefficient for coaxial probe model

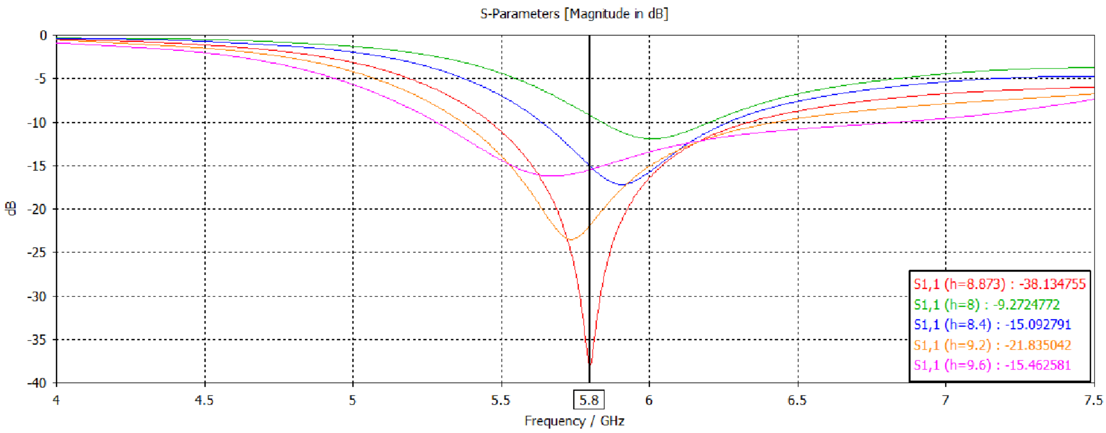

Fig. 4.9: Effect of altering height of the DR on Reflection coefficient for coaxial probe model

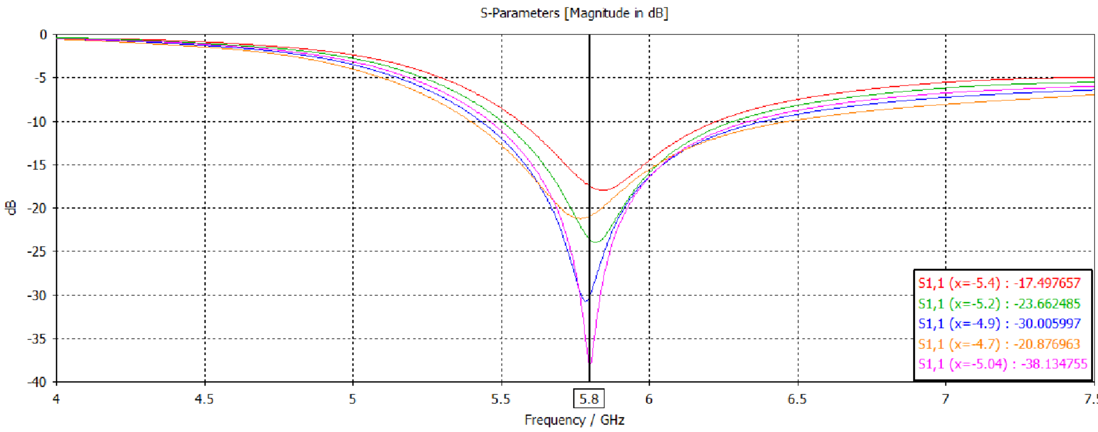

Fig. 4.10: Effect of altering probe length l_p by x mm on Reflection coefficient for coaxial probe model

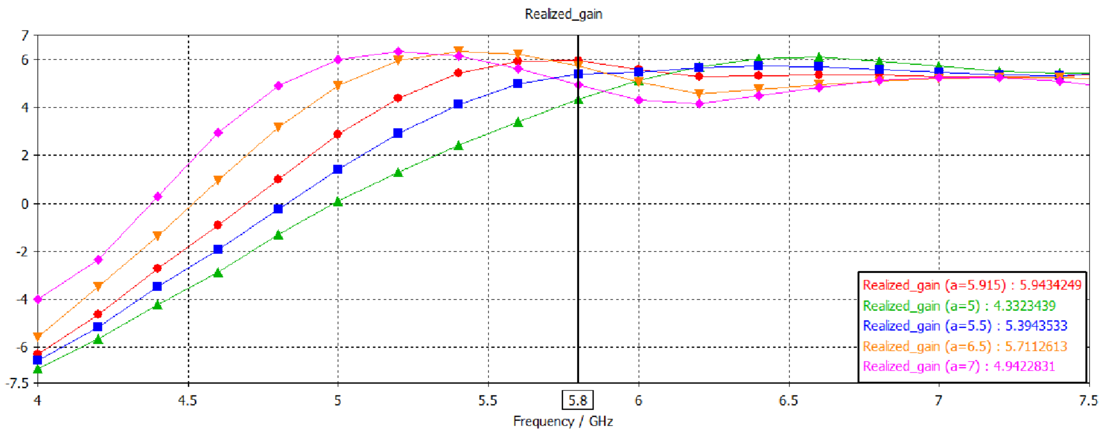

Fig. 4.11: Effect of altering radius of DR on realized gain of the coaxial probe model

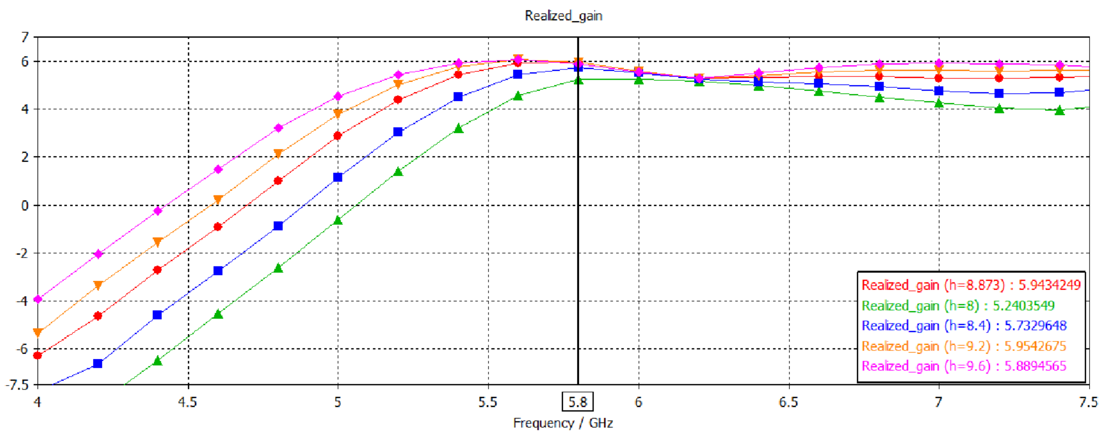

Fig. 4.12: Effect of altering height of DR on realized gain for coaxial probe model

4.3 Aperture coupled CDRA

This section describes the design of the model with aperture coupling. Simulation results are presented and the parametric study is conducted.
The aperture slot is cut on the ground plane, where the DR is mounted (Fig. 4.13), and it is fed by a 50Ω microstrip line. The aperture has initial dimensions of length $l_a = 7.737mm$, width $w_a = 1.547mm$. The microstrip feed line has the width of $w_f = 2.91mm$ and the thickness of $mt = 0.035mm$. The dimensions of the microstrip line were chosen in such way that it is matched to an impedance of 50Ω, using the macro function for calculating line impedance in CST microwave studio. Initial physical parameters of the aperture coupled model are summarized in Tab. 4.2. The following equations where used to determine the initial dimensions of the aperture [12]:

$$l_a = \frac{0.4\lambda_0}{\sqrt{\varepsilon_e}} = \frac{0.4\lambda_0}{\sqrt{\frac{\varepsilon_r+\varepsilon_s}{2}}} = \frac{0.4 \times 0.051724}{\sqrt{\frac{10+4.3}{2}}} = 7.737\ mm, \tag{4.1}$$

$$w_a = 0.2l_a = 0.2 \times 7.737 = 1.547mm \tag{4.2}$$

Additionally, the microstrip line is adjusted by a stub extension s so that its reactance cancels out that of the slot [12].

$$s = \frac{\lambda_g}{4} = \frac{28.638}{4} = 7.16mm \tag{4.3}$$

λ_g is the guided wave in the substrate given by [6, 12]:

$$\lambda_g = \frac{\lambda_0}{\sqrt{\varepsilon_{eff}}} = \frac{0.051724}{\sqrt{3.262}} = 28.638mm \tag{4.4}$$

ε_{eff} is the effective dielectric constant given by equation 4.5 [6]. However, in this case, ε_{eff}=3.262 mm was verified by the macro function in CST microwave studio.

$$\varepsilon_{eff} = \frac{\varepsilon_s + 1}{2} + \frac{\varepsilon_s - 1}{2}\left[1 + 12\frac{h}{W}\right]^{\frac{-1}{2}} \tag{4.5}$$

4.3.1 Simulated results for aperture coupled CDRA

The antenna configuration with initial parameters defined in Tab. 4.2 did not achieve the desired results, therefore the dimensions of the feed line and the slot were slightly adjusted. The stub extension s was optimized to 7.17 mm, w_a to 1.6 mm.

Tab. 4.2: Initial dimensions of the aperture coupled model

Parameter	**Value [mm]**
Radius of the resonator a	5.6
Height of the resonator h	10.0
Length of the slot l_a	7.737
Width of the slot w_a	1.547
Stub extension s	7.16

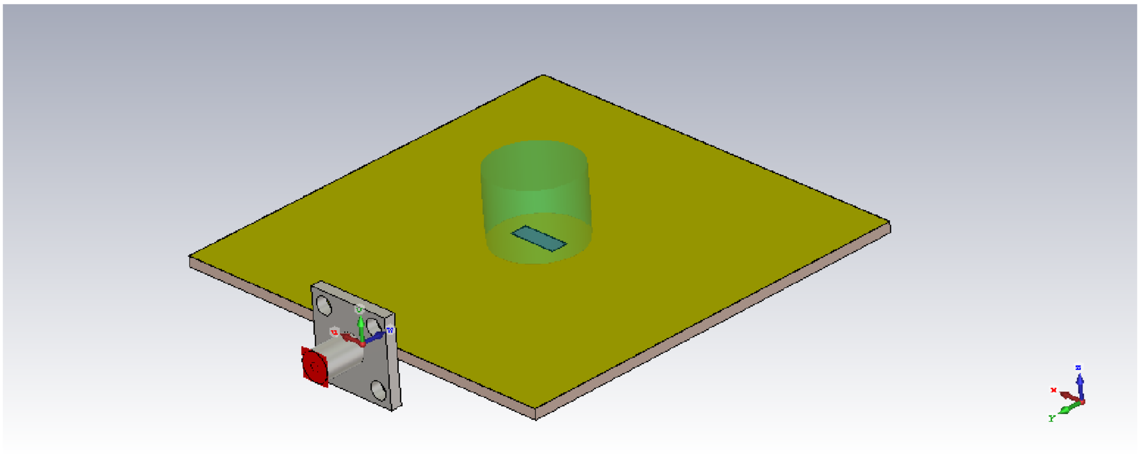

Fig. 4.13: Numerical model of the aperture coupled CDRA

Fig. 4.14 shows optimized results for the reflection coefficient. At resonant frequency (5.8 GHz), the antenna achieved the realized gain of 5.089 and total efficiency of 79.4% (see Fig.4.15 and 4.16. This model, however, shows quite strong backward radiation, as compared to the case of coaxial probe (Fig. 4.18 and 4.7).

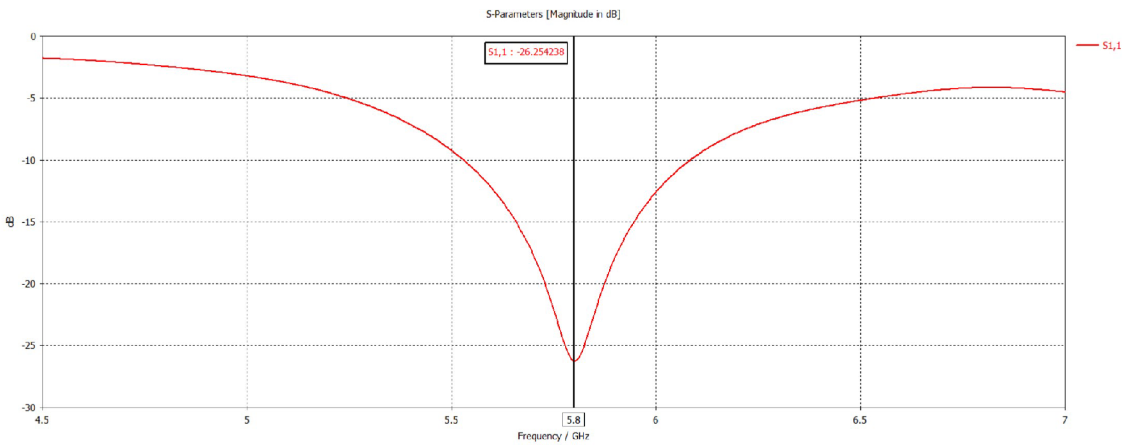

Fig. 4.14: Reflection coefficient for aperture coupled model

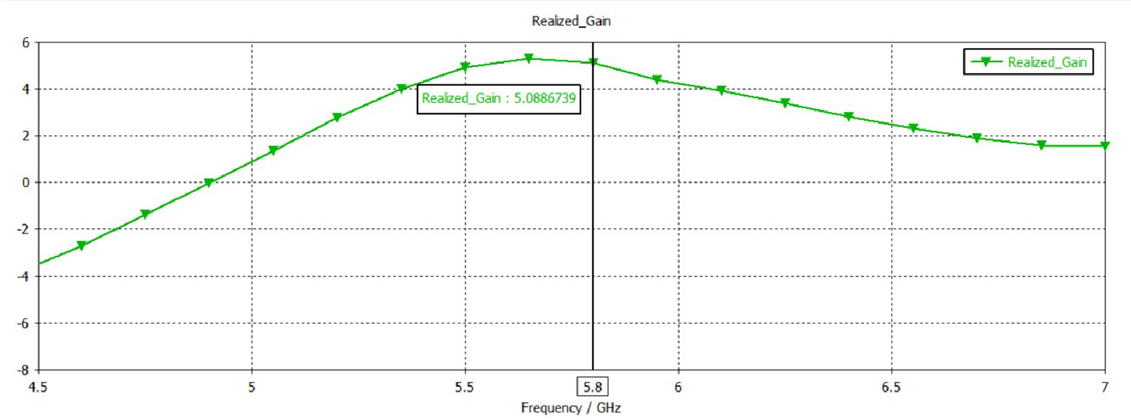

Fig. 4.15: Realized gain for aperture coupled model

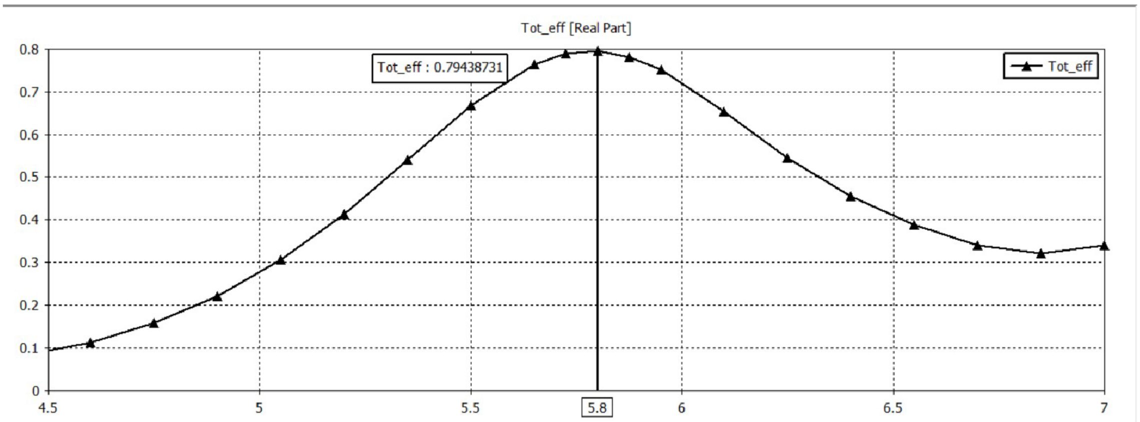

Fig. 4.16: Total efficiency for aperture coupled model

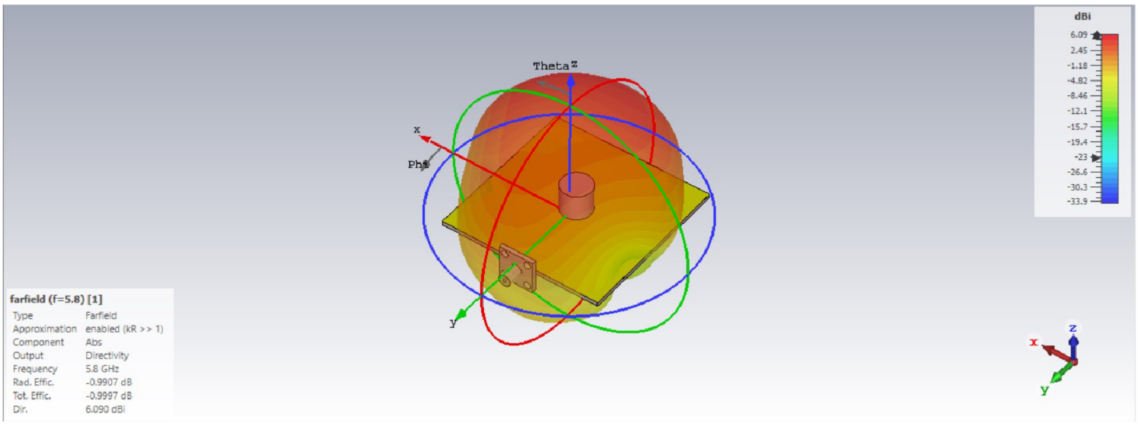

Fig. 4.17: 3D radiation pattern at 5.8GHz for aperture coupled model

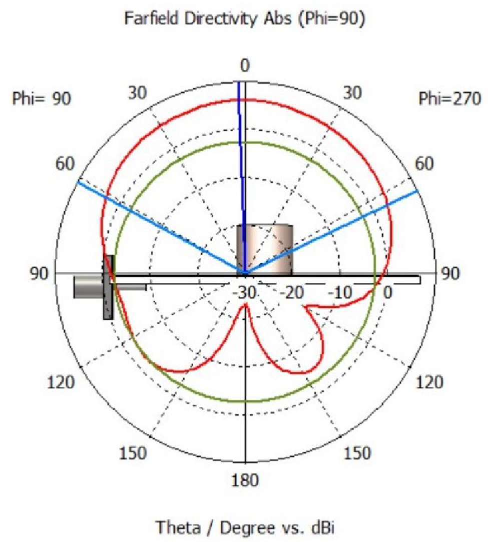

(a) Absolute gain

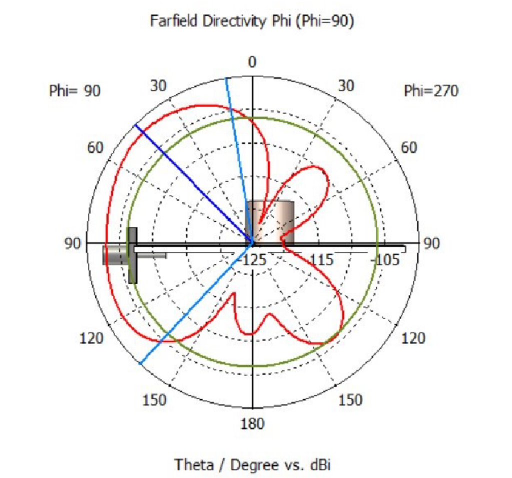

(b) Phi component

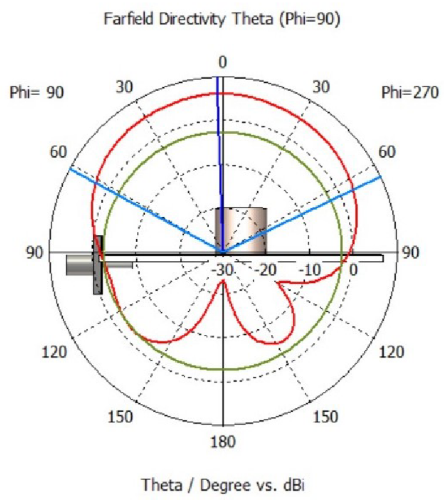

(c) Theta component

Fig. 4.18: Radiation pattern of the aperture coupling model

4.3.2 Parametric analysis of the aperture coupled model

As it was witnessed in section 4.2.2, altering physical parameters of the dielectric resonator greatly affect the performance of the antenna. Fig. 4.20 and 4.19, show the effects of altering radius a and height h on the resonant frequency of the antenna.

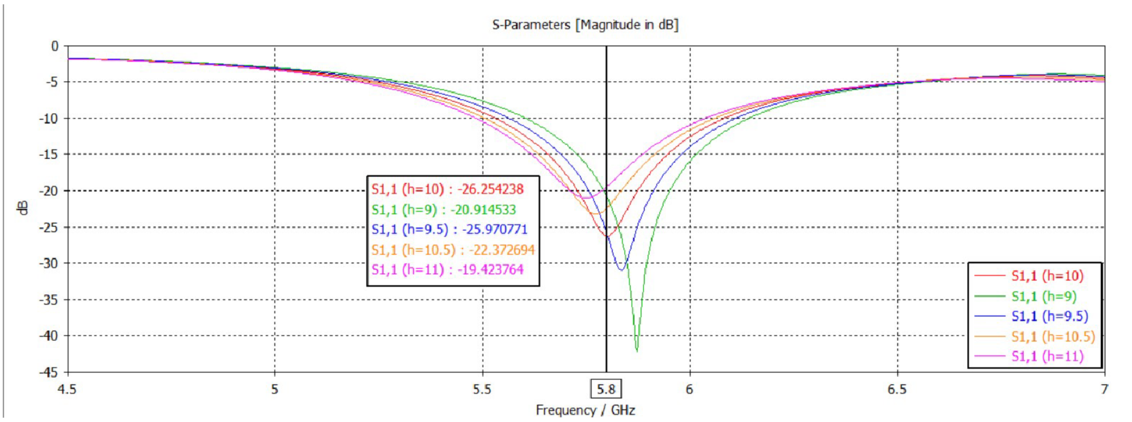

Fig. 4.19: Effect of varying height of DR on reflection coefficient of CDRA

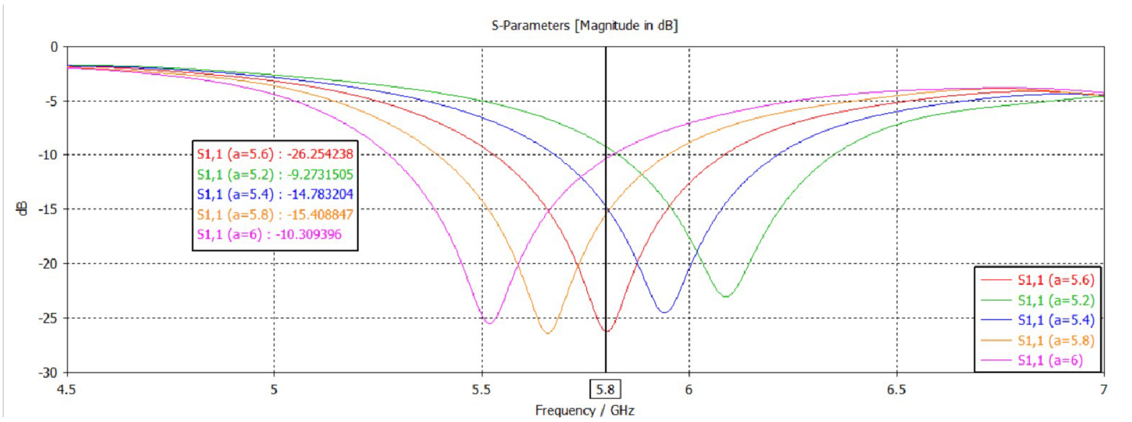

Fig. 4.20: Effect of varying radius of DR on reflection coefficient of CDRA

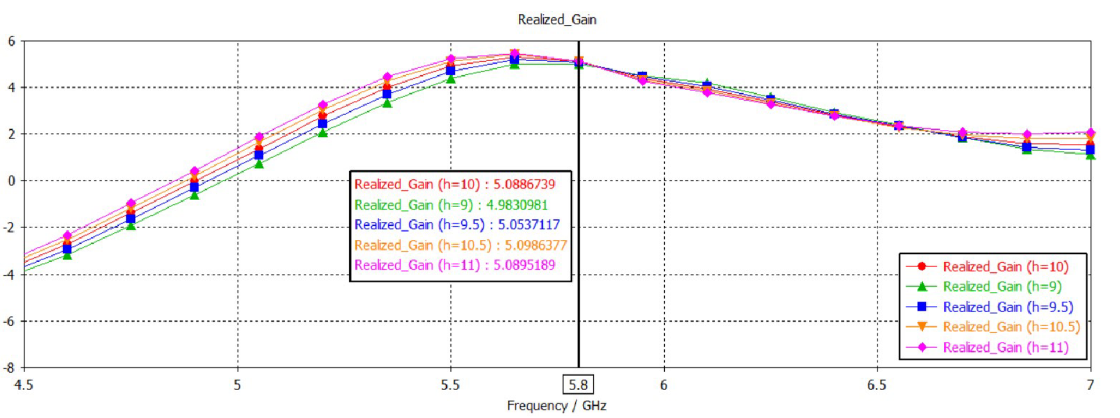

Fig. 4.21: Effect of altering the height of the DR on realized gain

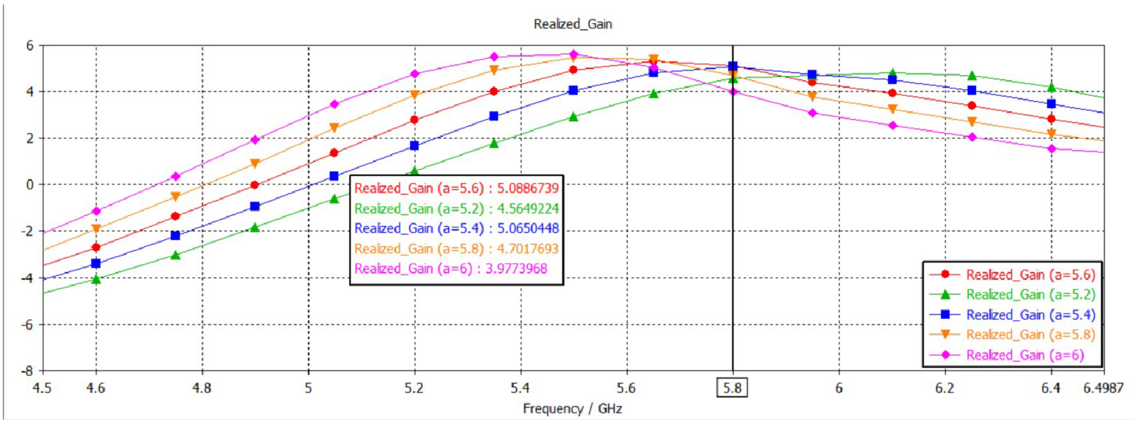

Fig. 4.22: Effect of altering radius of the DR on realized gain

4.4 Comparison of performance between coaxial probe and aperture coupled models of the CDRA

In both models, desirable results were achieved. The parametric study shows that alteration to the physical parameters of the DR as well as the feeding structure greatly affect the characteristics of the CDRA. The effect is greatly observed on the shift to the operating frequency. Gain and total efficiency in both scenarios was maximum at the working frequency, however, the coaxial probe configuration presented slightly better results as compared to the aperture coupled model. A summarized comparison of achieved results is given in Tab. 4.3.

Tab. 4.3: Comparison of achieved results for coaxial probe and aperture coupling

Description	**Aperture coupled model**	**Coaxial probe model**
Gain[dBi]	5.0887	5.943
Total efficiency [%]	79.44	95.91
|S11| [dB]	-26.254	-38.125
BW[%] ($\|S11\| < -10$)	18.1	15.08

5 Manufacturing and measurements

In this chapter, all steps relating to the fabrication and measurement process of the proposed antenna are presented. From the designs made in chapter 4, the aperture coupled model (section 4.3) was chosen for implementation, due to its simplicity in the fabrication process, as no extra drilling is required. The selected model was then optimized for fabrication by fine-tuning the dimension of the slot using *trusted region framework algorithm* in CST studio.

Tab. 5.1: Dimensions of the optimized aperture coupled model

Parameter	**Value [mm]**
Radius of the resonator a	5.6
Height of the resonator h	10.0
Length of the slot l_a	8.0
Width of the slot w_a	2.0

5.1 Simulation of manufacturing process

In any manufacturing industry, almost non of the production processes is 100% perfect, therefore, even in this project, it is important to take into account uncertainties that may result from the fabrication process on the properties of the antenna. Among many factors, the prominent factors that may affect the performance of the resulting antenna considered in this thesis are namely: change in dielectric constant of the material for the dielectric resonator, the position of the DR relative to the slot and glue thickness for mounting the DR.

As it can be seen in Fig. 5.1, the reduction in dielectric constant of the material used for the DR would alter the performance of the antenna. The reduction in dielectric constant of the material is usually encountered in 3D printing, material extrusion 3D printing technique in particular, because in most cases the filling of material may not be 100% [23].

Moving the dielectric resonator away from the center of the slot, not only result in the shift of the resonant frequency but also worsen the performance of the antenna in comparison to the ideal scenario (Fig. 5.2).

Additionally, glue tape used for fixing the dielectric resonator on the ground plane may also result in poor performance of the antenna as it may contribute to the overall reduction in dielectric constant of the material. However, if well mounted, the effect may be minimal as the glue layer is relatively thin.

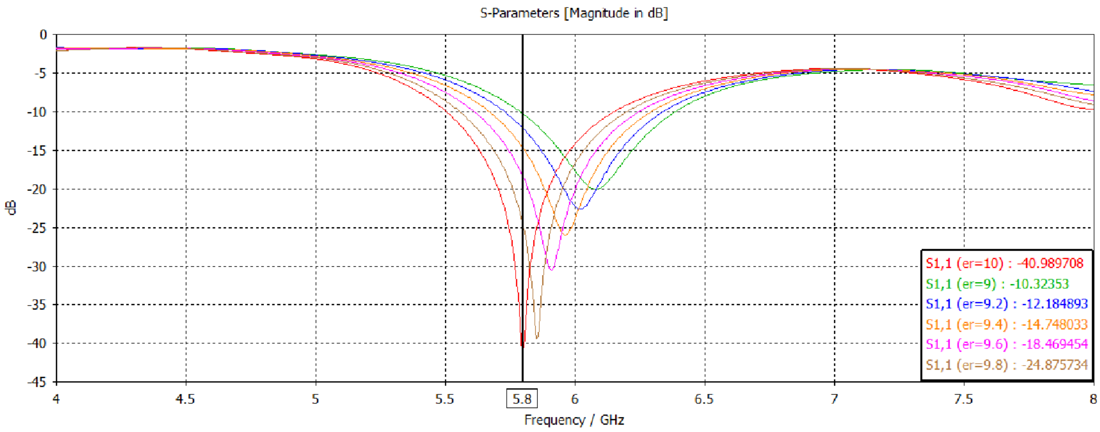

Fig. 5.1: Errors resulting in reduction in dielectric constant of the materials due to manufacturing tolerance.

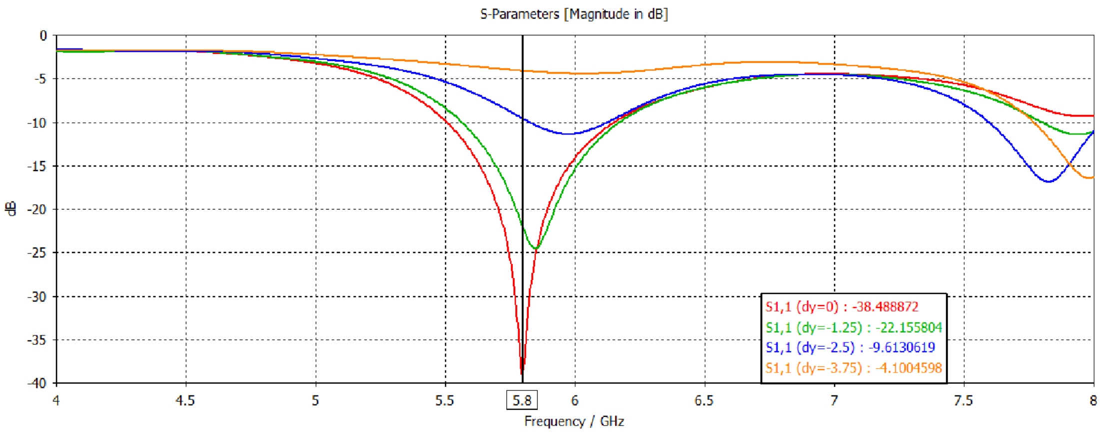

Fig. 5.2: Performance errors that may result from improper fixing of the DR on the board.

5.2 Fabrication of prototypes

The dielectric resonators for the antenna were fabricated from Perperm 3D ABS1000 filament material, which has the data-sheet dielectric constant of $\varepsilon_r = 10$, loss tanget $\tan\delta = 0.003$, using Prusa i3 MK3S 3D printing machine. Fabrication was done in three versions due to errors encountered with the initial model and a total of four dielectric resonators were printed in each version with different profile filling of materials, namely concentric, rectilinear, archimedean chords and octagram spirals (Fig. 5.3). The dielectric resonators were then mounted on square board using a double-sided glue tape, which has a thickness of $\approx 50\mu$m and the dielectric constant $\varepsilon_r = 3$.

The board on which the dielectric resonators were mounted, were made from FR-4 substrate, which has the dielectric constant of $\varepsilon_s = 4.3$ with a thickness of 1.52mm. The board were laminated with a thin layer of copper on top (copper thickness 0.035mm), which forms the ground plane, on which the rectangular slot was cut. The resulting antenna is fed by a 50Ω located at the bottom (Fig. 5.4).

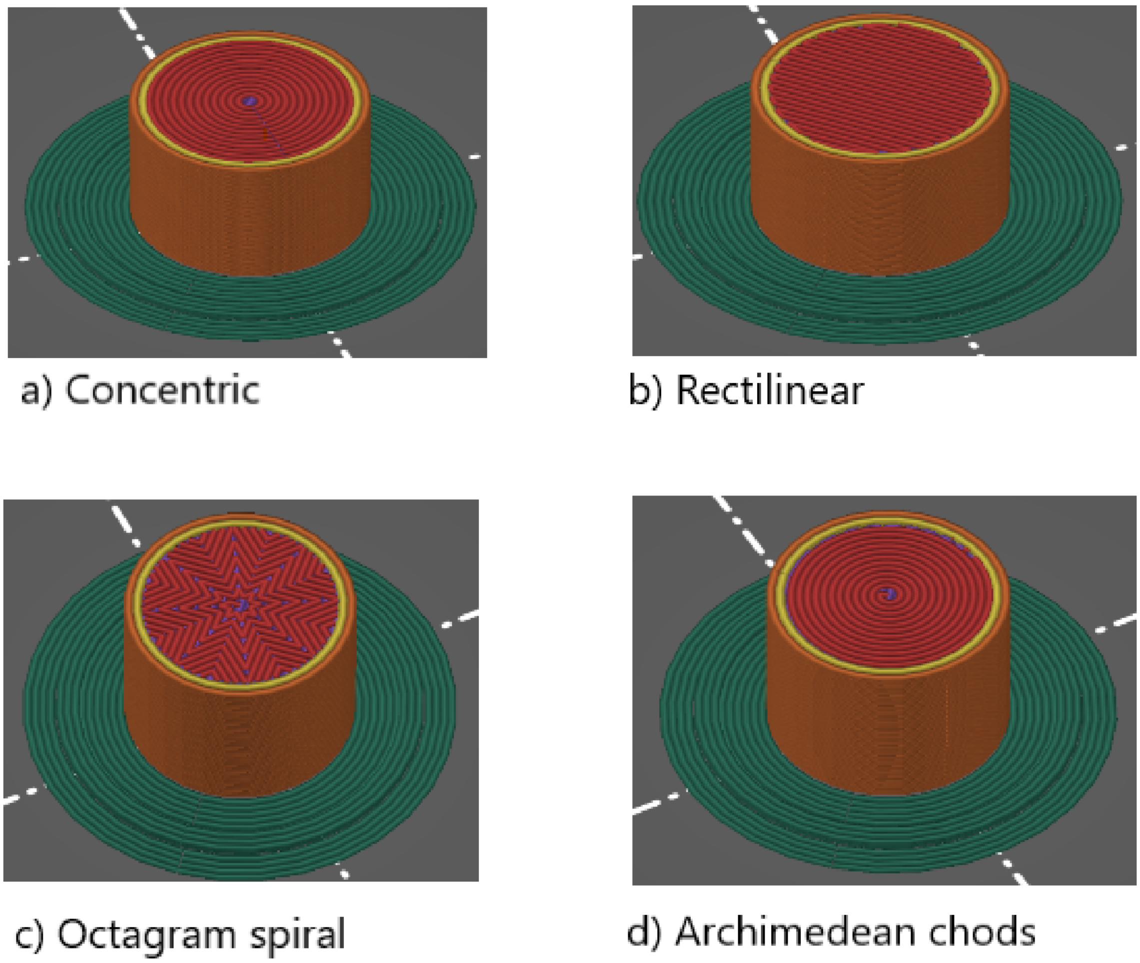

Fig. 5.3: Different 3D printing profiles.

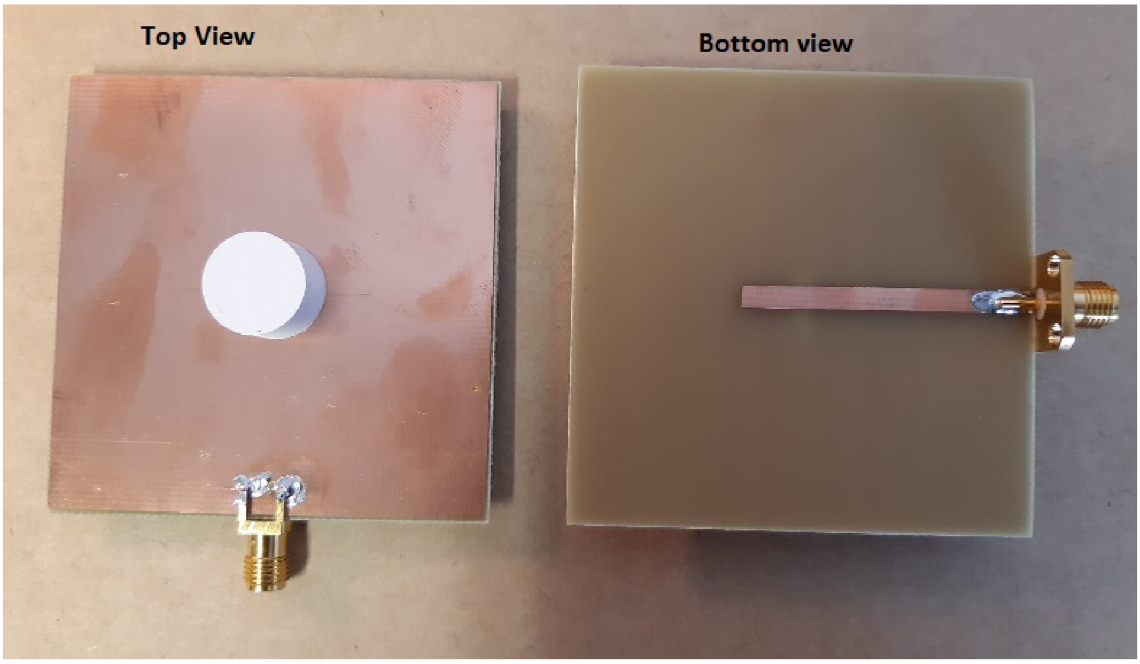

Fig. 5.4: Top and bottom view of the assembled antenna prototype.

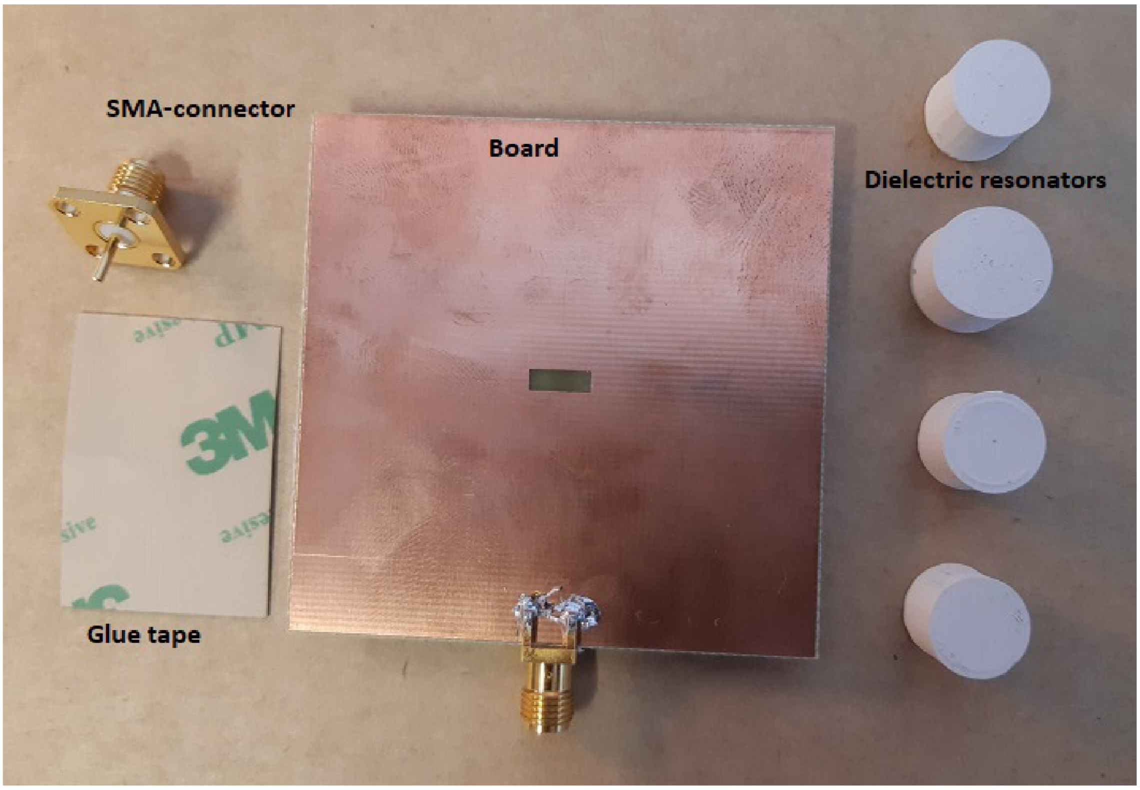

Fig. 5.5: Unassembled antenna parts.

5.3 Measurements and discussion of achieved results

Measurements of the properties of the real antenna were conducted in the school laboratory at the department of Radioelectronics. The reflection coefficient were measured using a vector network analyzer and measurements of the radiation characteristics were conducted in the anechoic chamber.

5.3.1 Alpha version

Measurements of the reflection coefficient for the *alpha* version of the antenna resulted in error as the achieved results were shifted outside the target working frequency band of ISM 5.8 GHz. The *alpha* version is based on optimized antenna dimensions given in Tab. 5.1. As it can be seen in Fig. 5.6, a divide of two groups was created, with one group comprising of the models with rectilinear and concentric printing profiles resonating at $f_r \approx 6.46$GHz and another group made of archimedean and octagram profile fillings resonating at $f_r \approx 6.6$Ghz. The difference in behaviour between the two groups of printing profiles, may have been caused by the fact that some profiles are printed as a solid line over each layer and some as many sub-lines.

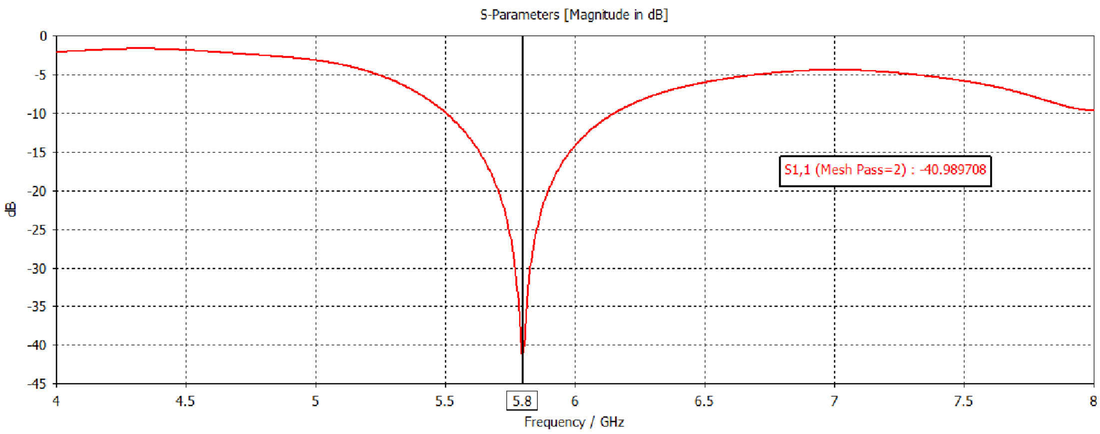

Fig. 5.6: simulated reflection coefficient for the optimized *alpha* model

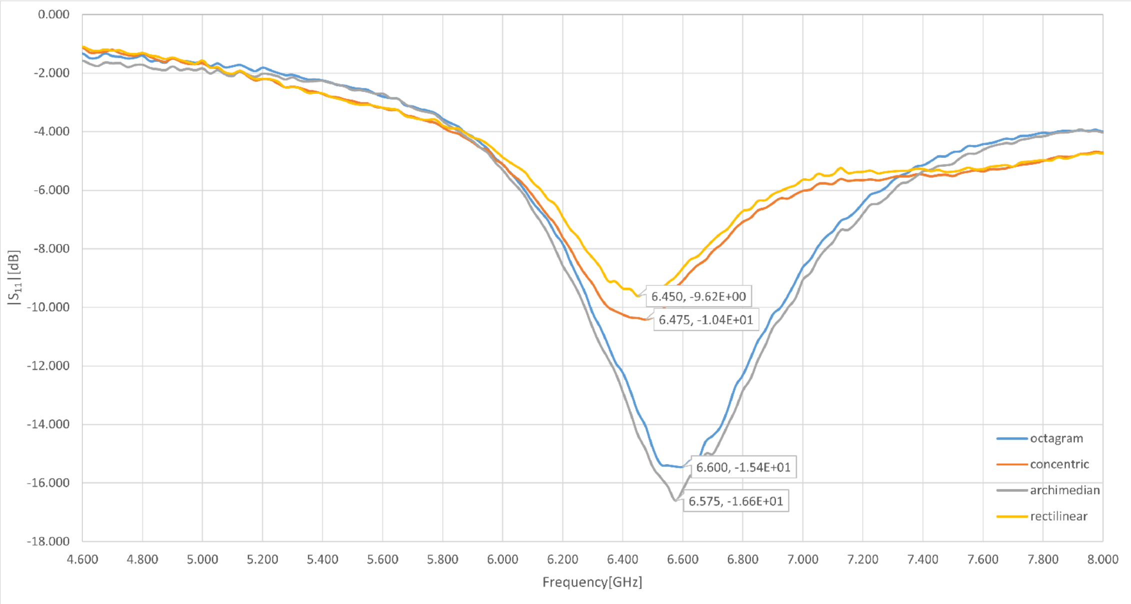

Fig. 5.7: Measured reflection coefficient for four different printing infill

5.3.2 Beta version

Tab. 5.2 shows the dimensions for the reconfigured antenna models with new dielectric constants ε_r. The simulated reflection coefficient of the reconfigured antenna models are depicted in Fig. 5.8 and 5.10. The new values of the dielectric constants were arrived at by parametric analysis of ε_r in CST Microwave studio, taking results realized in *alpha* version as reference.

Tab. 5.2: Dimensions of reconfigured models with new dielectric constants ε_r

Parameter	**Model00** ($\varepsilon_r = 7.7$)	**Model01** ($\varepsilon_r = 7.9$)
Radius of the DR a [mm]	7.03	6.75
Height of the DR h [mm]	8.5	9.0
Length of the slot l_a [mm]	8.0	8.0
Width of the slot w_a [mm]	2.0	2.0

Results in the *beta* version for reflection coefficient (Fig: 5.9 and 5.11), are control results achieved by investigating the cause of frequency shift in the *alpha* version. Comparing the results with those achieved in *alpha* version (Fig. 5.7), it was learnt that the reduction in dielectric constant ε_r of the material from which the dielectric resonator was printed was way bigger than what was expected. Tab. 5.3 and 5.4 give a summary of achieved results for the four profile infills in comparison with simulated results.

Tab. 5.3: Comparison of achieved results for *beta* models with $\varepsilon_r = 7.7$

Description	**Archimedean**	**Octagram**	**Simulated results**
|S11| [dB]	-11.2	-12.08	-15.16
BW [%] ($\|S11\| < -10$)	4.00	4.93	8.45
f_r [GHz]	5.838	5.81	5.8

Tab. 5.4: Comparison of achieved results for *beta* models with $\varepsilon_r = 7.9$

Description	**Concentric**	**Rectilinear**	**Simulated results**
|S11| [dB]	-10.24	-11.02	-16.17
BW [%] ($\|S11\| < -10$)	2.41	4.14	8.62
f_r [GHz]	5.86	5.84	5.8

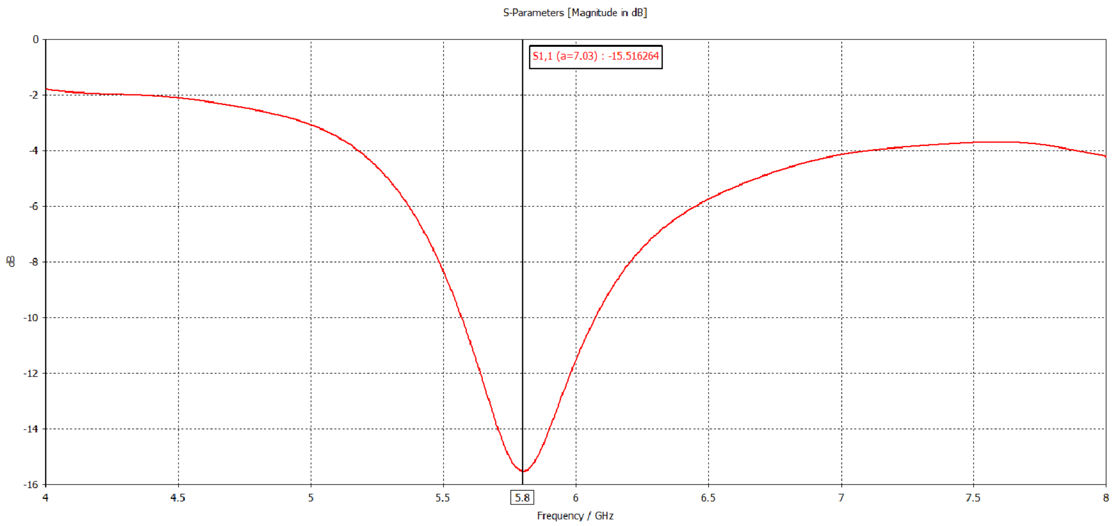

Fig. 5.8: simulated reflection coefficient for the reconfigured *beta* model with $\varepsilon_r = 7.7$

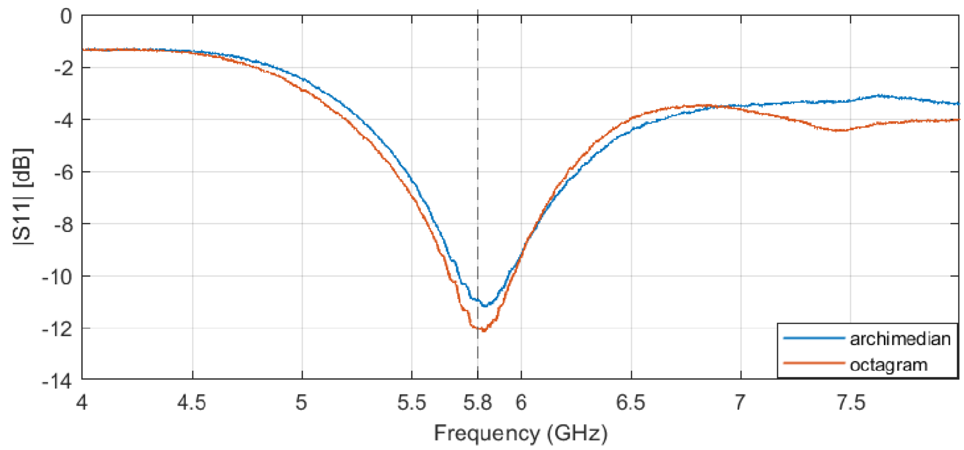

Fig. 5.9: Measured reflection coefficient for archimedian and octagram infill ($\varepsilon_r = 7.7$)

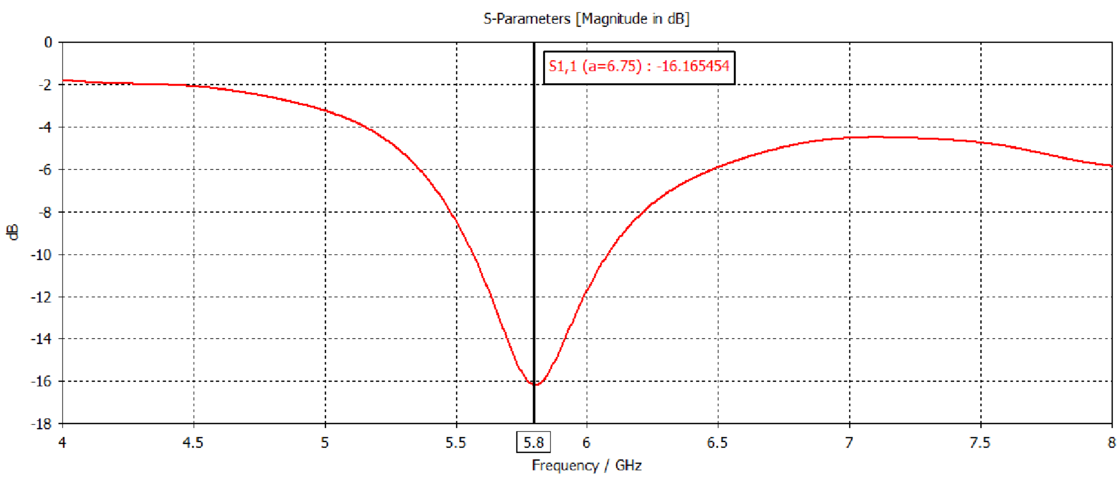

Fig. 5.10: simulated reflection coefficient for the optimized *beta* model with $\varepsilon_r = 7.9$

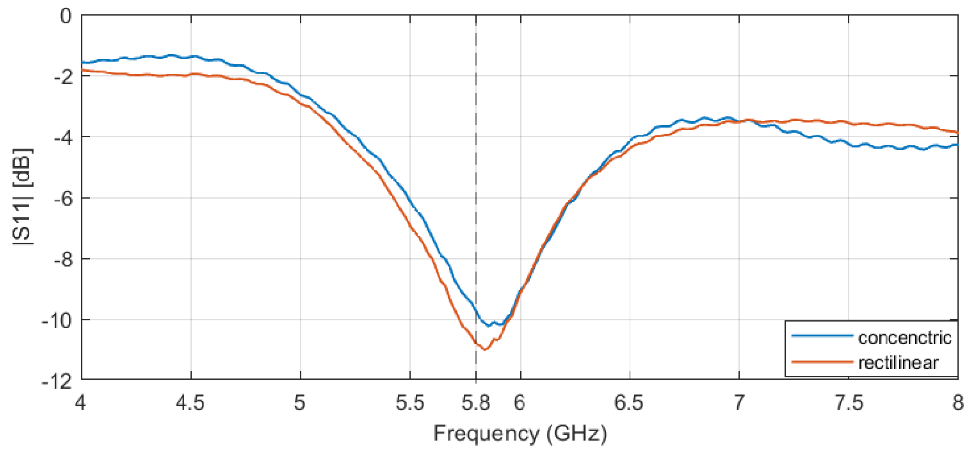

Fig. 5.11: Measured reflection coefficient for concentric and rectilinear infill ($\varepsilon_r = 7.9$)

5.3.3 Final version

Finally, upon confirming the range for the dielectric constant of the real antenna models in *beta* version, the models of the antenna were reconfigured and optimized for optimal performance (see Fig.5.5). In CST *Trust region framework algorithm* was used to optimized the antenna models. In the final version, both reflection coefficient and radiation characteristics of the antenna were measured.

Tab. 5.5: Optimized dimensions of reconfigured models with new values of ε_r

Parameter	**Model00** ($\varepsilon_r = 7.7$)	**Model01** ($\varepsilon_r = 7.9$)
Radius of the DR a [mm]	6.512	6.72
Height of the DR h [mm]	10.0	9.0
Length of the slot l_a [mm]	8.64	7.021
Width of the slot w_a [mm]	2.47	2.238
Stub extension s [mm]	3.16	4.05

Reflection coefficient

The measured and optimized simulated reflection coefficient results of the antenna models are shown in Fig. 5.12 and 5.13. Comparing measured results to simulations, 3 out of 4 antennas performed very well. The best performance was observed for the model with rectilinear printing profile, which achieved $|S11| \approx -31.246$dB at 5.804GHz against simulated model with $|S11| = -33.699$dB at 5.8 GHz, the working bandwidth is $\approx 15.69\%$, which is identical to simulation results (See Fig. 5.13). The worst performance quantified by the reflection coefficient was observed on the model with octagram spirals with resonance frequency f_r at ≈ 6.0GHz , which is outside the frequency band for which the antenna was designed (see Fig. 5.12). Achieved results for all models are summarised in Tab. 5.6 and 5.7.

Tab. 5.6: Comparison of achieved results for models with $\varepsilon_r = 7.7$

Description	**Archimedean**	**Octagram**	**Simulated results**
|S11| [dB]	-35.54	-23.99	-62.4
BW [%] ($\|S11\| < -10$)	23.45	26.43	24.14
f_r [GHz]	6.02	5.796	5.8

Tab. 5.7: Comparison of achieved results for models with $\varepsilon_r = 7.9$

Description	**Concentric**	**Rectilinear**	**Simulated results**
|S11| [dB]	-26.725	-31.219	-33.699
BW [%] ($\|S11\| < -10$)	14.69	16.4	14.86
f_r [GHz]	5.832	5.804	5.8

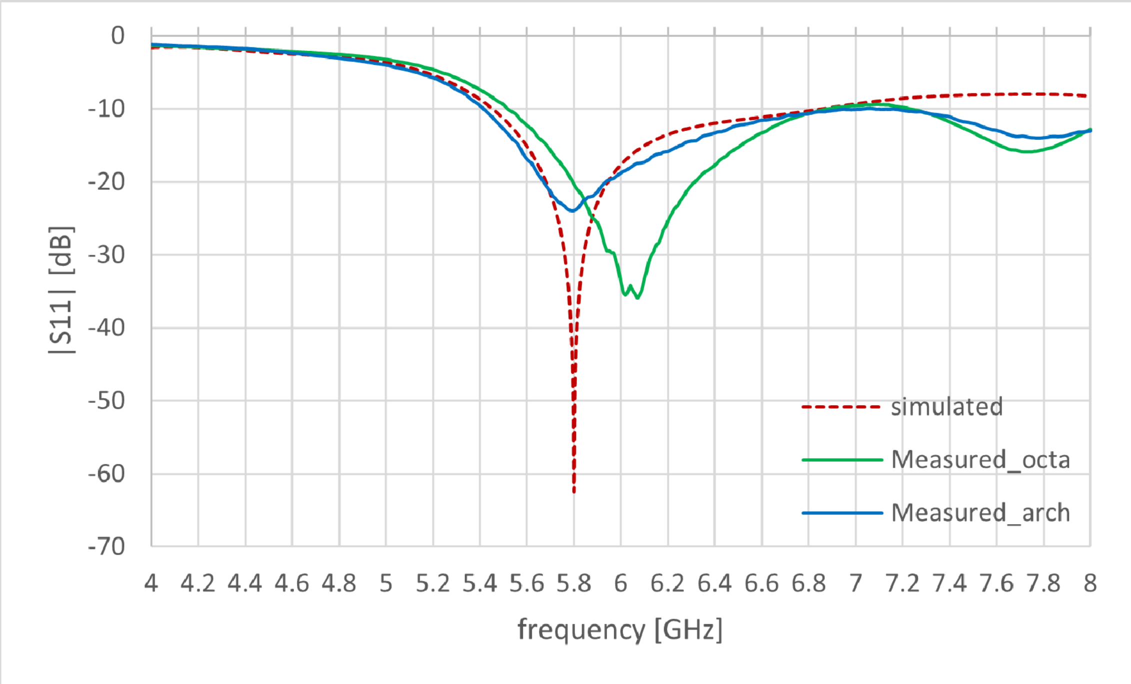

Fig. 5.12: Measured reflection coefficient for archimedean and octagram infill (final)

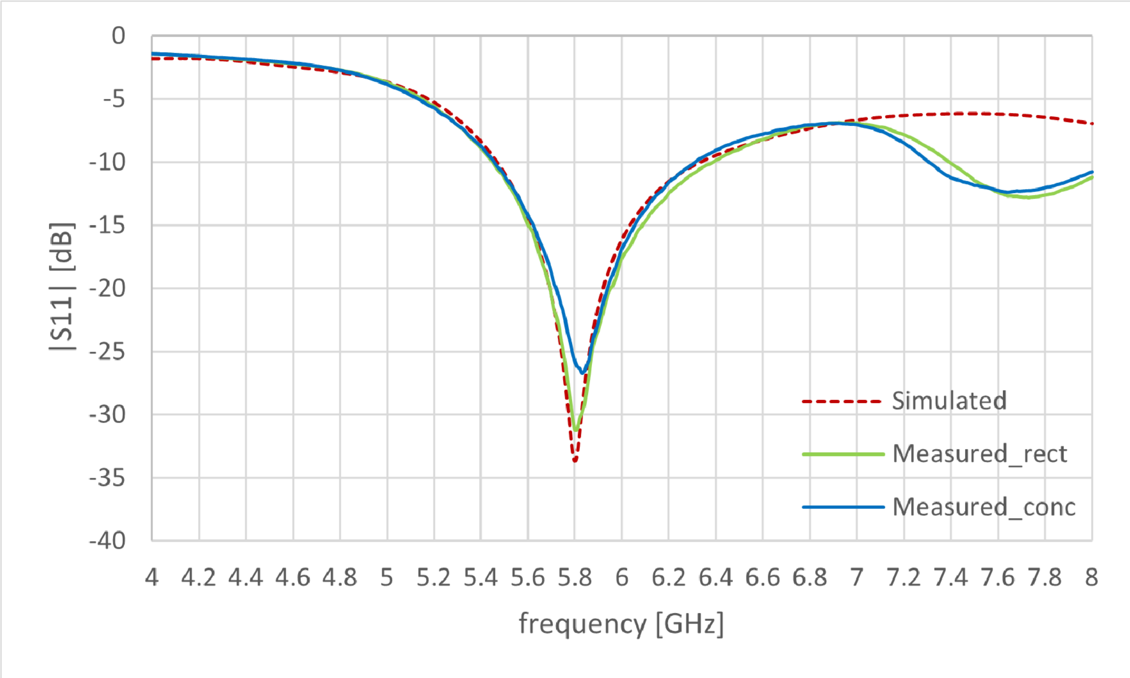

Fig. 5.13: Measured reflection coefficient for concentric and rectilinear infill (final)

Radiation characteristics

The measured and simulated normalized radiation patterns of the of the antenna models are depicted in Fig. 5.14, through Fig. 5.21. The radiation pattern was measured only for two prototypes out of the four fabricated antennas, antenna with rectilinear infill representing configuration with $\varepsilon_r = 7.9$ and the one with archimedean chords representing the configuration with $\varepsilon_r = 7.7$. As it can be seen in figures below, measured and simulated radiation pattern agree in both planes (transversal and longitudinal) at 5.8 GHz for co-polarization, however do not agree for cross-polarization.

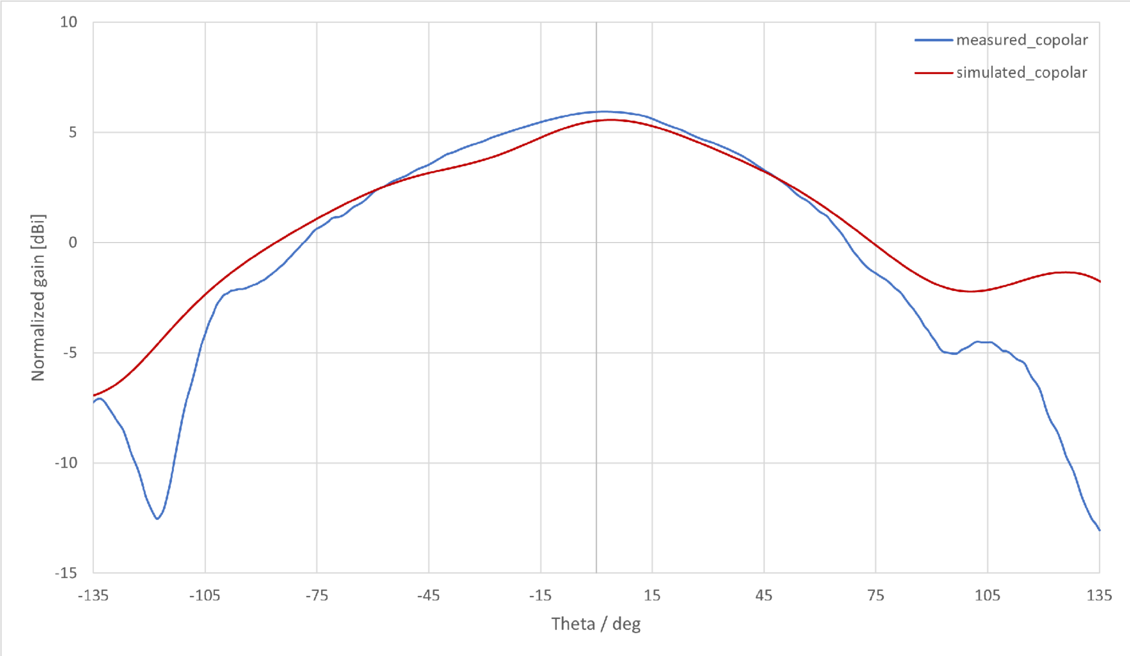

Fig. 5.14: Simulated and measured radiation characteristics at 5.8 GHz in longitudinal plane for rectilinear infill (co-polarized)

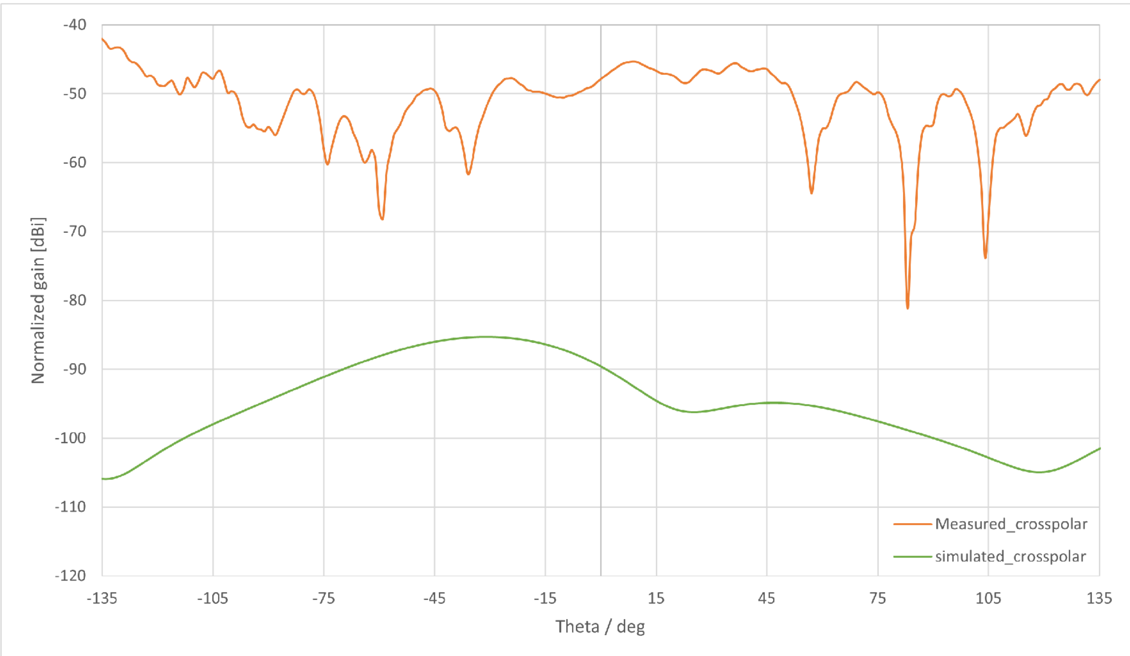

Fig. 5.15: Simulated and measured radiation characteristics at 5.8 GHz in longitudinal plane for rectilinear infill (cross-polarized)

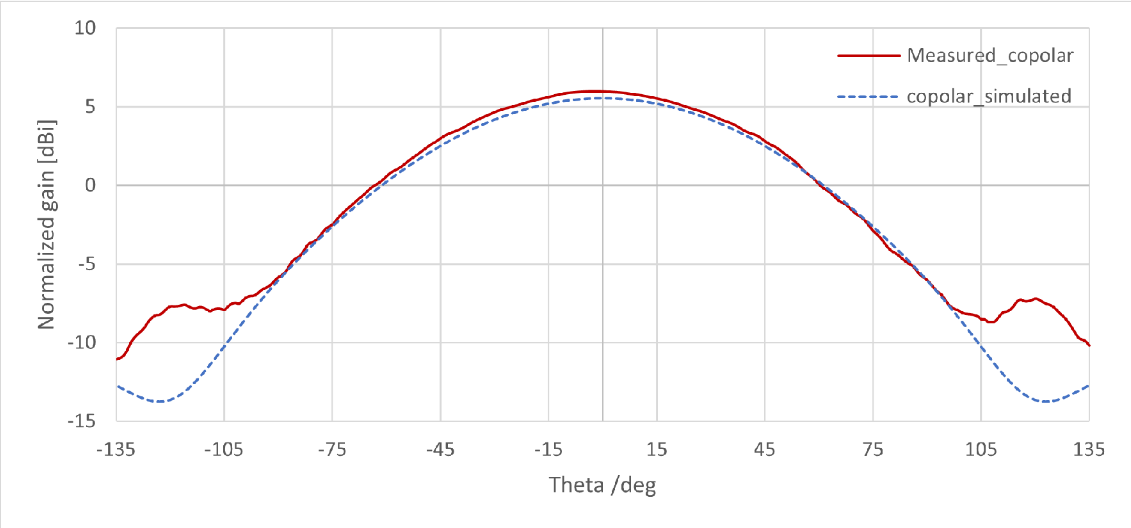

Fig. 5.16: Simulated and measured radiation characteristics at 5.8 GHz in transversal plane for rectilinear infill(co-polarized)

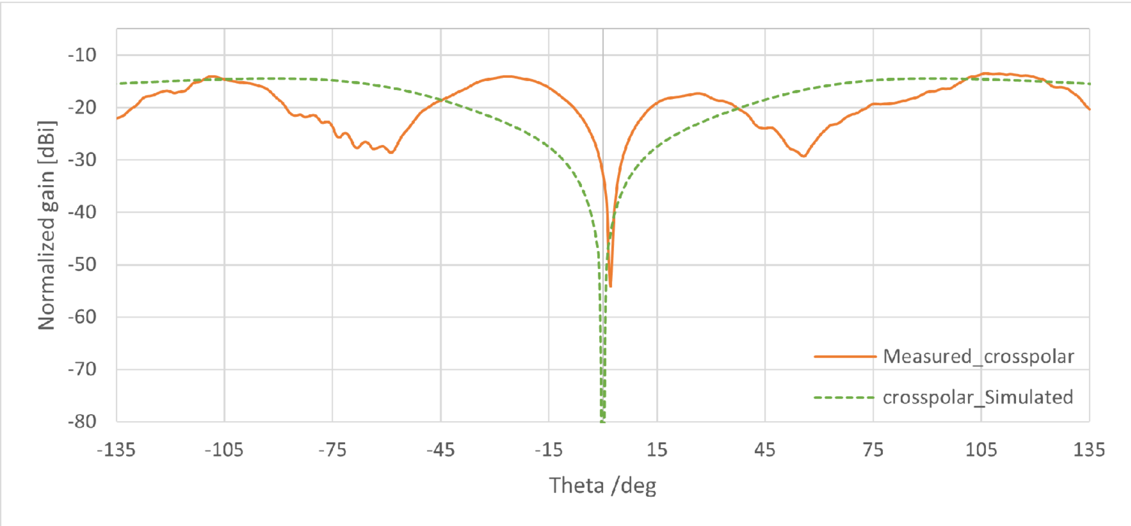

Fig. 5.17: Simulated and measured radiation characteristics at 5.8 GHz in transversal plane for rectilinear infill(cross-polarized)

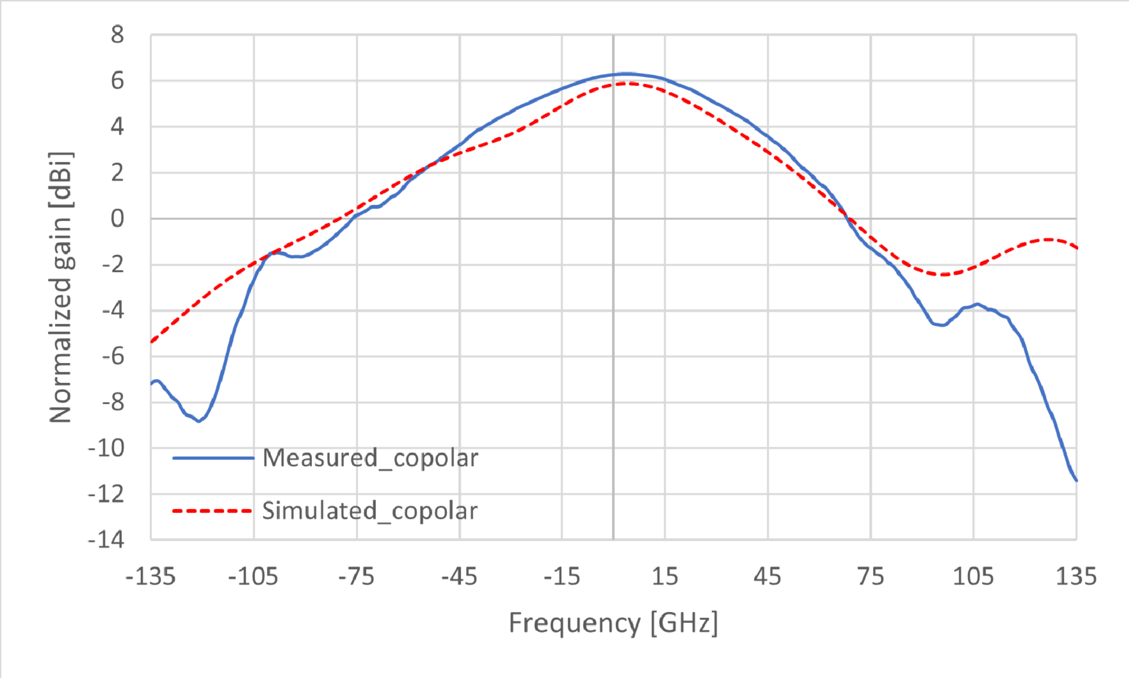

Fig. 5.18: Simulated and measured radiation characteristics at 5.8 GHz in longitudinal plane for archimedean chords(co-polarized)

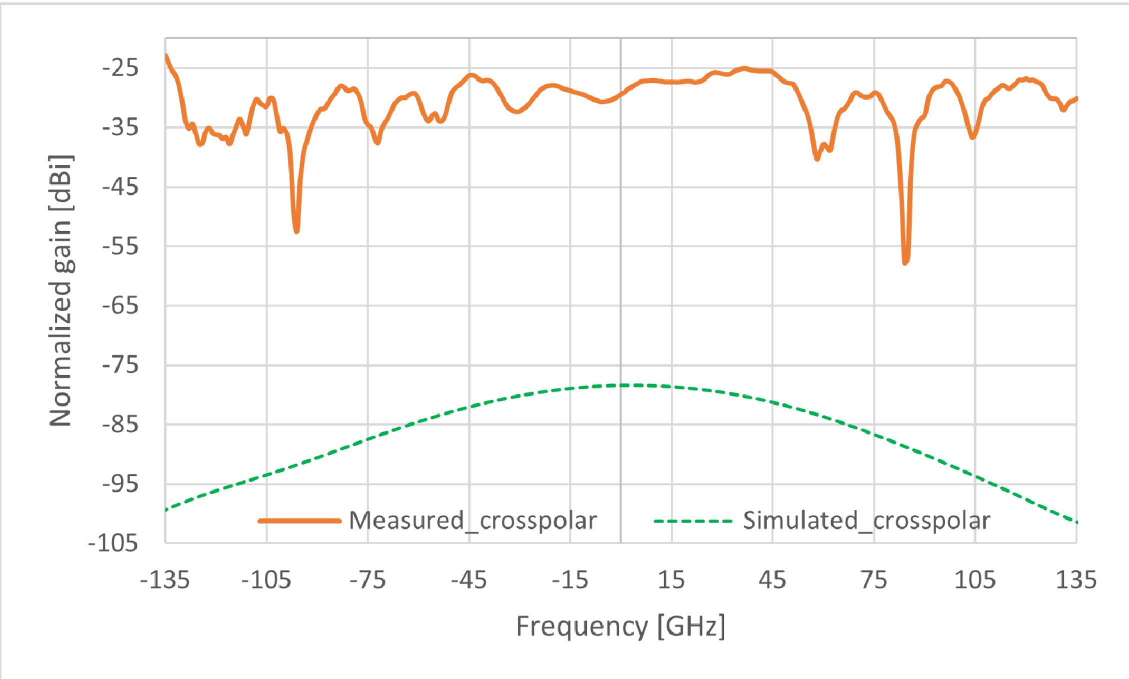

Fig. 5.19: Simulated and measured radiation characteristics at 5.8 GHz in longitudinal plane for archimedean chords(cross-polarized)

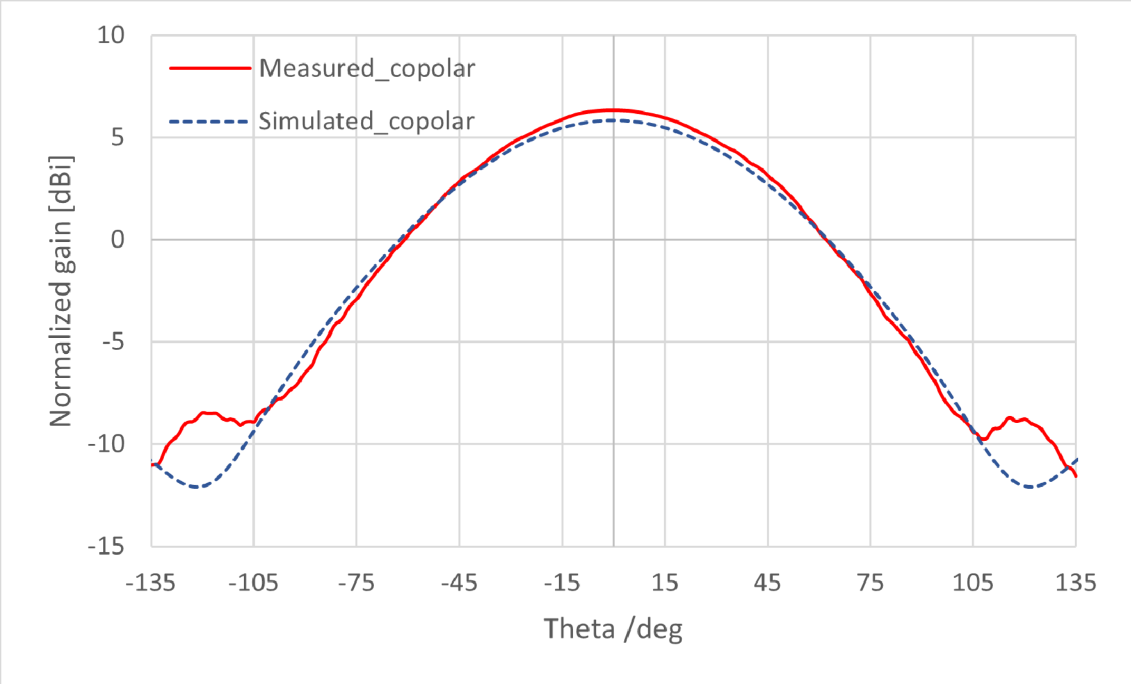

Fig. 5.20: Simulated and measured radiation characteristics at 5.8 GHz in transversal plane for archimedean chords(co-polarized)

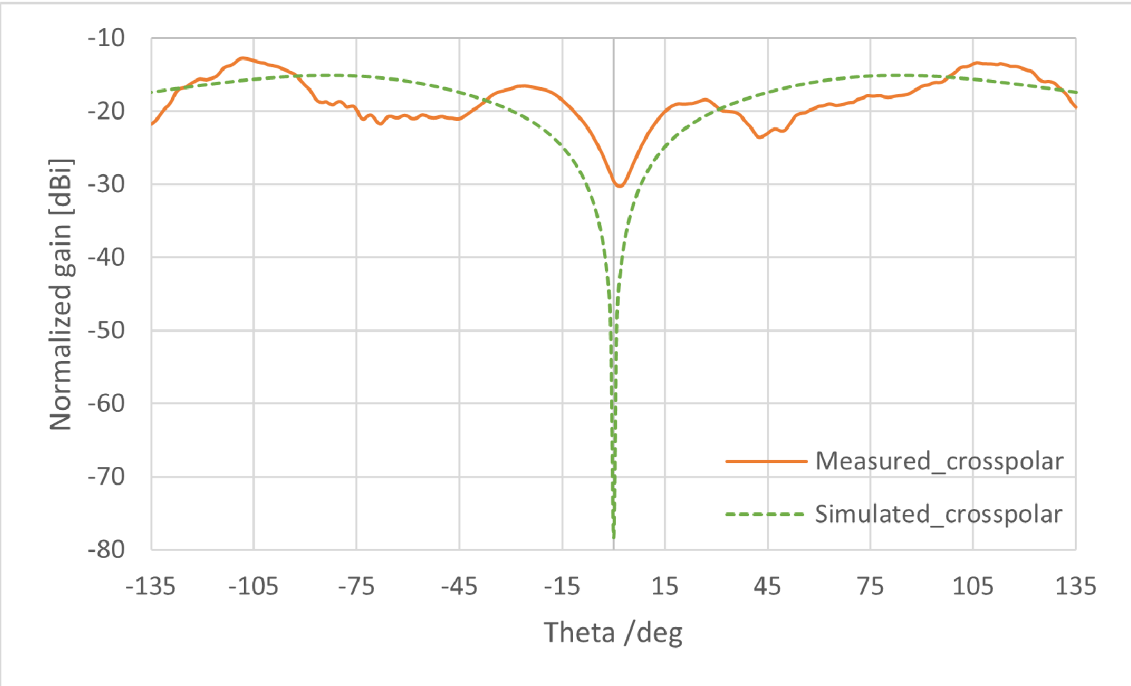

Fig. 5.21: Simulated and measured radiation characteristics at 5.8 GHz in transversal plane for archimedian chords(cross-polarized)

Conclusion

The aim of this bachelor's thesis was to design, investigated and fabricated a cylindrical dielectric resonator antenna operating at frequency band of ISM 5.8 GHz. The designed antenna was to be fabricated using 3D printing technology.

In the theoretical part of this thesis, an overview of the dielectric resonator antennas is given in chapter 1. Details and equation necessary for designing cylindrical dielectric resonator antennas are described in chapter 2. Additionally, an overview of 3D printing technology is presented in chapter 3.

In the second part of this thesis, two numerical models of the cylindrical dielectric resonator antenna were designed, one with aperture coupling and the other with coaxial probe coupling mechanism. The antenna models were designed in CST microwave studio. In the case of coaxial probe (Section 4.2), it was observed that the performance of the antenna is greatly affected by the length of the probe and its position relative to the DR. Similarly, the dimensions of the aperture slot affect the behavior of the model with aperture coupling. A parametric study revealed that altering physical parameters of the antenna cause a shift to the resonant frequency of the antenna. A comparison in performance between the two models is given in Tab. 4.3.

The aperture model of the designed antenna models was chosen for realization, due to its simplicity in fabrication as no drilling is required. The model was optimized and fabricated using Prusa i3 MK3S 3D printing machine using different material filling profiles and its parameter were measured.

The reflection coefficient of the antenna was measured using a vector network analyzer and the radiation pattern was measured in the anechoic chamber. During measurements, the initial results resulted in error, due to unexpected manufacturing tolerance. The error resulted in the shift of the of the operating frequency to position outside the target ISM 5.8 GHz band, hence the results were unusable (Fig. 5.7). Following an investigation, it was learnt that the error was caused by the reduction in dielectric constant of the material from which the dielectric resonator was printed (section 5.3.2). The antenna model was then the reconfigured and optimized with new values of the dielectric constant and measured (section 5.3.3). After reconfiguration, good results were achieved, among the four material profile infills (Fig. 5.3), the prototype with rectilinear profile achieved the best overall results. The rectilinear model achieved the resonant frequency of 5.804 GHz ($|S11|$ = -31.219 dB), compared to the target simulated resonant frequency of 5.8GHz ($|S11|$= -33.699 dB). The worst performance was recorded on the model with octagram spirals, whose resonant frequency was outside the ISM 5.8 GHz frequency band (Fig. 5.6).

Bibliography

[1] Rajveer S. Yaduvanshi and Harish Parthasarathy. *Rectangular Dielectric Resonator Antennas*. Springer New Delhi, New Dehli, 1st ed edition, 2016. doi:https://doi.org/10.1007/978-81-322-2500-3.

[2] K.M. Luk and K.W. leung. *Dielectric Resonator Antennas*. RESEARCH STUDIES PRESS LTD, Baldock, Hertfordshire, England, 2003.

[3] Raghvendra Kumar Chaudhary, Rajkishor Kumar, and Rakesh Chowdhury. *Circularly Polarized Dielectric Resonator Antennas*. Artech House, Norwood, MA 02062, 2021.

[4] S. Keyrouz and D. Caratelli. Dielectric resonator antennas. *International journal of antennas and propagation*, 2016:1–20, 2016. doi:10.1155/2016/6075680.

[5] Jitendra Kumar and Navneet Gupta. Performance analysis of dielectric resonator antennas. *Wireless personal communications*, 75(2):1029–1049, 2013. doi:https://doi.org/10.1007/s11277-013-1406-3.

[6] Constantine A Balanis. *Antenna theory*. Wiley, Hoboken, 4th ed edition, 2016.

[7] Ondřej Stříteský, Josef Průša, and Martin Bach. *Basics of 3D Printing with Josef Prusa*. Prusa Research a.s., Prague, 1st ed edition, 2019. URL: https://www.prusa3d.com/page/basics-of-3d-printing-with-josef-prusa_490/.

[8] 3d printing - additive, 2018. URL: https://make.3dexperience.3ds.com/processes/introduction-to-additive-processes.

[9] Lmr®-100a. URL: https://www.timesmicrowave.com/Products/Cables/LMR_%C2%AE_High_Performance_/Standard_LMR%C2%AE/LMR%C2%AE-100A/.

[10] Rajveer S Yaduvanshi and Gaurav Varshney. *Nano Dielectric Resonator Antennas for 5G Applications*. CRC Press, Milton, 2020. doi:10.1201/9781003029342.

[11] A. Faiz, Muhammad Shafique, N. Gogosh, Sahil Khan, and Mahmood Khan. Dual he11δ mode cdra for polarization diversity applications in k band point-to-point communications. *Radioengineering*, 29:521–528, 09 2020. doi:10.13164/re.2020.0521.

[12] Aldo Petosa. *Dielectric Resonator Antenna Handbook*. Artech House, Boston, 2007.

[13] Zhen-Xing Xia and Kwok Wa Leung. 3d-printed wideband rectangular dielectric resonator antenna. In *2019 Photonics Electromagnetics Research Symposium - Fall (PIERS - Fall)*, pages 285–289, 2019. doi:10.1109/PIERS-Fall48861.2019.9021330.

[14] Zhen-Xing Xia, Kwok Wa Leung, and Kai Lu. 3-d-printed wideband multi-ring dielectric resonator antenna. *IEEE Antennas and Wireless Propagation Letters*, 18(10):2110–2114, 2019. doi:10.1109/LAWP.2019.2938009.

[15] Francesco Paolo Chietera, Riccardo Colella, and Luca Catarinucci. Dielectric resonators antennas potential unleashed by 3d printing technology: A practical application in the iot framework. *Electronics*, 11(1), 2022. URL: https://www.mdpi.com/2079-9292/11/1/64, doi:10.3390/electronics11010064.

[16] Aldo Petosa and Apisak Ittipiboon. Dielectric resonator antennas. *IEEE antennas & propagation magazine*, 52(5):91–116, 2010. doi:10.1109/MAP.2010.5687510.

[17] K. W Leung, M. L Poon, W. C Wong, K. M Luk, and E. K. N Yung. Aperture-coupled dielectric resonator antenna using a strip-line feed. *Microwave and optical technology letters*, 24(2):120–121, 2000. doi:10.1002/(SICI)1098-2760(20000120)24:2120::AID-MOP113.0.CO;2-E.

[18] K.W Leung, K.M Luk, K.Y.A Lai, and D Lin. Theory and experiment of a coaxial probe fed hemispherical dielectric resonator antenna. *IEEE transactions on antennas and propagation*, 41(10):1390–1398, 1993. doi:10.1109/8.247779.

[19] Debatosh Guha, Poulomi Gupta, and Chandrakanta Kumar. Dualband cylindrical dielectric resonator antenna employing hem11δ and hem12δ modes excited by new composite aperture. *IEEE transactions on antennas and propagation*, 63(1):433–438, 2015. doi:10.1109/TAP.2014.2368116.

[20] Debatosh Guha, Archita Banerjee, Chandrakanta Kumar, Yahia M. M. Antar, and M. T. Sebastian. Design guidelines for the cylindrical dielectric resonator antenna using the recently proposed hem12d mode [antenna designer's notebook]. *IEEE Antennas and Propagation Magazine*, 56(4):148–158, 2014. doi:10.1109/MAP.2014.6931672.

[21] N. Shahrubudin, T.C. Lee, and R. Ramlan. An overview on 3d printing technology: Technological, materials, and applications. *Procedia Manufacturing*, 35:1286–1296, 2019. The 2nd International Conference on Sustainable Materials Processing and Manufacturing, SMPM 2019, 8-10 March 2019, Sun City,

South Africa. URL: https://www.sciencedirect.com/science/article/pii/S2351978919308169, doi:https://doi.org/10.1016/j.promfg.2019.06.089.

[22] 3d printing technology guide, 2021. URL: https://all3dp.com/1/types-of-3d-printers-3d-printing-technology/.

[23] Matias Cuevas, Francisco Pizarro, Ariel Leiva, Gabriel Hermosilla, and Daniel Yunge. Parametric study of a fully 3d-printed dielectric resonator antenna loaded with a metallic cap. *IEEE Access*, 9:73771–73779, 2021. doi:10.1109/ACCESS.2021.3081068.

Symbols and abbreviations

f_{r}	resonant frequency
ε_{r}	Dielectric constant of the material
ε_{s}	Dielectric constant of the substrate
l_{a}	Length of the aperture slot
w_{a}	Width of the aperture slot
λ_0	Free space wavelength
c	Speed of light in free space
S11	Reflection coefficient
BW	Bandwidth
CDRA	Cylindrical dielectric resonator antenna
DRA	Dielectric resonator antenna
DR	Dielectric resonator

A Assignment in Czech language

The next page contains the assignment in Czech language (the original language of the study program).

VYSOKÉ UČENÍ TECHNICKÉ V BRNĚ
FAKULTA ELEKTROTECHNIKY A KOMUNIKAČNÍCH TECHNOLOGIÍ

Bakalářská práce

bakalářský studijní program **Elektronika a komunikační technologie**

Ústav radioelektroniky

Student: Masauso Lungu ***ID:*** 209533
Ročník: 3 ***Akademický rok:*** 2021/22

NÁZEV TÉMATU:

3D tištěná dielektrická rezonátorová anténa

POKYNY PRO VYPRACOVÁNÍ:

Seznamte se s principem a návrhem dielektrických rezonátorových antén a možnostmi jejich buzení. V programu CST Microwave Studio vytvořte numerický model válcové dielektrické rezonátorové antény pro kmitočtové pásmo ISM 5,8 GHz. Zkoumejte vliv různých typů buzení antény na její vlastnosti. Po dohodě s vedoucím práce vyberte vhodný typ buzení a dokončete návrh antény.

U navržené antény modelujte vliv výrobního procesu na parametry antény. Anténu vyrobte pomocí technologie 3D tisku s využitím různých tiskových profilů. Pak anténu změřte a výsledky srovnejte s výsledky simulací.

DOPORUČENÁ LITERATURA:

[1] PETOSA, A., Dielectric Resonator Antenna Handbook. Boston: Artech House, 2007. Artech House Antennas and Propagation Library. ISBN 1-59693-206-6.
[2] PROCHÁZKA, M., Antény: encyklopedická příručka. 2. vyd. Praha: BEN - technická literatura, 2001. ISBN 80-7300-028-8.

Termín zadání: 11.2.2022 ***Termín odevzdání:*** 1.6.2022

Vedoucí práce: Ing. Jaroslav Zechmeister

doc. Ing. Lucie Hudcová, Ph.D.
předseda rady studijního programu

B Data-sheet of SMA connector

The next page contains a data-sheet of the SMA connect used, when designing the antenna models in this thesis.

REV.	DATE	DESCRIPTION
A	05/01/04	UPDATE DRAWING FORMAT
B	10/10/07	REMOVE CRIMP NOTES

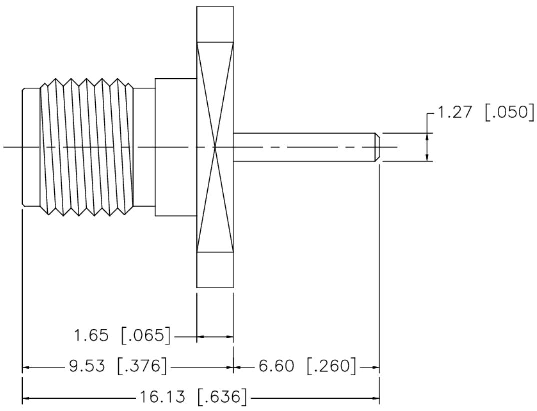

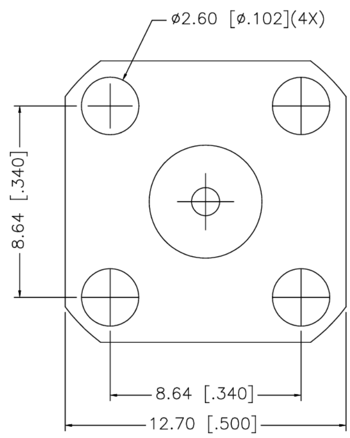

8				
7				
6				
5				
4				
3	CONTACT PIN	BER. COPPER	GOLD	1
2	INSULATOR	TEFLON	NATURAL	1
1	BODY	BRASS	GOLD	1
	DESCRIPTION	MATERIAL	FINISH	QTY

UNLESS OTHERWISE SPECIFIED DIMENSIONS ARE IN MILLIMETERS. DIMENSIONS IN [ ] ARE IN INCHES AND FOR CUSTOMER REFERANCE ONLY.

UNLESS OTHERWISE SPECIFIED TOLERANCES FOR MILLIMETERS ARE:
0.5 – 8mm ± 0.20mm
8 – 30mm ± 0.40mm
30 – 120mm ± 0.50mm

UNLESS OTHERWISE SPECIFIED TOLERANCES FOR INCHES ARE:
.020 – .315 = ± 0.007"
.315 – 1.180 = ± 0.015"
1.180 – 4.724 = ± 0.020"

DO NOT SCALE DRAWING

APPROVALS		DATE
DRAWN	G.R.S.	10/10/07
CHECKED		
ISSUED		
SHEET	1 OF 1	
CAD FILE	C:/132/132204.DWG	

Amphenol Connex

PART DESCRIPTION
SMA PANEL RECEPT. JACK

PART NO.
132204

DWG. NO.	REV.	SIZE	SCALE
132204.DWG	B	A	NA